waste

MDPI

Article

Physico-Mechanical Properties of an Aluminosilicate Refractory Castable Obtained After Chamotte Waste Recycling by Firing Method

Leonel Díaz-Tato, Jesús Fernando López-Perales, Yadira González-Carranza, José Eulalio Contreras de León and Edén Amaral Rodríguez-Castellanos *

Facultad de Ingeniería Mecánica y Eléctrica (FIME), Universidad Autónoma de Nuevo León (UANL), San Nicolás de los Garza 66450, Mexico; leonel.diazat@uanl.edu.mx (L.D.-T.); jlopezp@uanl.edu.mx (J.F.L.-P.); yadira.gonzalezcn@uanl.edu.mx (Y.G.-C.); jose.contrerasle@uanl.edu.mx (J.E.C.d.L.)
* Correspondence: eden.rodriguezcs@uanl.edu.mx or earc22@hotmail.com; Tel.: +52-818-329-4020

Abstract

Developing sustainable ceramic formulations that integrate industrial by-products addresses the high energy and raw material demands of refractory manufacturing while advancing circular economy goals. This study investigates the recycling of chamotte waste from rejected fired electrical porcelain as a partial substitute (5 and 10 wt.%) for flint clay in aluminosilicate refractory castables. Samples were fired at 110, 815, 1050, and 1400 °C and evaluated for bulk density, apparent porosity, cold crushing strength, and flexural strength. Microstructural and mineralogical changes were analyzed by SEM and XRD. Incorporating 10 wt.% chamotte waste fostered an in situ mullite-reinforced microstructure, enhancing mechanical strength (58 MPa—CCS, 18.8 MPa—MOR) and lowering porosity (24.4%), demonstrating chamotte's dual role as recycled raw material and reinforcement phase for densification and durability. These properties matched or surpassed those of the conventional formulation, with strength improvements of up to 44%. The findings demonstrate that high-temperature industrial waste can be effectively valorized in advanced refractories, reducing reliance on virgin raw materials, diverting waste from landfills, and promoting industrial symbiosis within the ceramics and metallurgical sectors.

Keywords: chamotte porcelain waste; refractory castables; sustainable; recycling; mechanical properties; mullite; anorthite

check for updates

Academic Editors: Krzysztof Pielichowski, Piotr Duda, Michał Łach, Tomasz Mariusz Majka, Tomasz Zdeb and Giovanni De Feo

Received: 30 August 2025
Revised: 26 September 2025
Accepted: 8 October 2025
Published: 17 October 2025

Citation: Díaz-Tato, L.; López-Perales, J.F.; González-Carranza, Y.; Contreras de León, J.E.; Rodríguez-Castellanos, E.A. Physico-Mechanical Properties of an Aluminosilicate Refractory Castable Obtained After Chamotte Waste Recycling by Firing Method. *Waste* **2025**, *3*, 35. https://doi.org/10.3390/waste3040035

Copyright: © 2025 by the authors. Licensee MDPI, Basel, Switzerland. This article is an open access article distributed under the terms and conditions of the Creative Commons Attribution (CC BY) license (https://creativecommons.org/licenses/by/4.0/).

1. Introduction

Refractory castables have become increasingly important in industrial applications over recent decades, largely due to their advantages over traditional fired bricks. These monolithic refractories can be cast and hardened at room temperature, offer flexibility in installation, and often present lower manufacturing costs. Such attributes have made them attractive for diverse high-temperature sectors, including metallurgy, cement production, and energy generation [1,2]. Table 1 shows a comparative summary of commercial aluminosilicate refractory castables: physical properties, mechanical performance, thermal behavior, phases, and microstructural features. Values represent typical ranges compiled from reported literature and industrial practice [3–16].

Table 1. Comparative summary of commercial aluminosilicate refractory castables.

Characteristic/Parameter	High-Alumina Cement Castable	Medium-Cement Castable	Low-Cement/Ultra-Low Cement Castable
Typical bulk density ($g \cdot cm^{-3}$)	2.7–3.3	2.5–3.0	2.3–2.8
Apparent porosity (%)	15–28	18–30	20–35
Cold compressive strength (CCS, MPa)	80–250	50–150	30–100
Cold modulus of rupture (MOR, MPa)	15–40	10–30	6–20
Hot MOR/strength (e.g., 1000–1400 °C)	5–30	3–20	1–12
Typical maximum continuous service temperature (°C)	1600–1750 (mullite/corundum systems)	1400–1600	1200–1400
Characteristic linear thermal expansion ($10^{-6} \cdot k^{-1}$)	3–6 (mullite-rich)	4–8	6–10 (more silica/glass influence)
Representative melting/softening behavior	High refractoriness; softening >~1800 °C; corundum stable	Softening range variable (may form low-viscosity phases near 1500–1650 °C if fluxed)	Lower softening temperature (glass-rich phases) ~1400–1550 °C
Principal crystalline phases after firing	Mullite (primary), corundum, minor cristobalite/glass	Mullite, anorthite, corundum, cristobalite, glassy phase	Cristobalite/quartz, anorthite/glass, limited mullite
Typical microstructural features	Interlocked mullite needles; corundum skeleton; relatively low pore connectivity when well sintered	Mixed mullite/anorthite matrix with partial liquid-phase sintering; moderate densification	Glassy matrix with dispersed crystalline phases; higher open porosity unless optimized
Advantages	Highest refractoriness and mechanical stability at very high temperature; proven for severe service	Balanced performance and cost; good at moderate-high temperature	Cost-effective for moderate temperature; easier workability
Limitations/risks	Higher material cost; more energy to manufacture	May form fluxed phases if impurities high	Lower refractoriness and mechanical capacity at high temperature
Typical industrial applications	Steel ladles, glass tank skirts, high-temperature kilns	Cement kilns, furnaces, glass forehearths (moderate-high temperature zones)	Biomass boilers, recuperators, low-temperature furnace linings
Design/processing considerations	Low water demand, high-temperature densification; careful aggregate grading	Control of CaO and fluxes to prevent excessive liquid phase	Minimize glass content where high temperature needed; optimize binder system
Environmental/economic note	High performance but higher embodied energy per kg	Trade-off between cost and performance	Lower embodied energy; lower cost

In aluminosilicate refractory castables, the primary raw materials typically include kaolinite clays, sillimanite minerals, and bauxites, chosen for their purity, abundance, and thermal stability [17,18]. However, these materials are sourced almost exclusively from finite natural deposits. The increasing global demand for refractories—combined with competition from other ceramic industries for the same raw materials—has raised concerns about the long-term sustainability of these mineral resources [19,20].

Integration of Secondary Resources in Refractory Castables

The integration of secondary raw materials into refractory formulations is not merely desirable but increasingly essential to advance sustainable development goals [21,22]. While ultra-low- and no-cement castables are often positioned as high-performance solutions, conventional and medium-cement systems remain more accessible, cost-effective, and reliable for low- to mid-temperature applications such as biomass-fueled boilers. In such systems, operating typically below 1100 °C, castables based on fired clay, mullite, and quartz provide adequate performance, with quartz contributing to the formation of a protective glassy phase that mitigates alkali corrosion [23,24].

Recent investigations reinforce the potential of by-products as functional additives. For instance, Škamat et al. (2024) demonstrated that partial substitution of calcined clay with 3–7 wt.% fly ash cenospheres in medium-cement castables enhanced thermal shock and alkali resistance, particularly at 5 wt.%, owing to optimized porosity and the development of mullite, cristobalite, and glassy phases [23]. Nevertheless, despite these encouraging outcomes, the systematic use of industrial by-products as full or partial replacements for fine aggregates in dense refractory castables remains underexplored. Expanding this line of research could unlock both performance gains and significant environmental benefits through reduced reliance on virgin raw materials.

Lately, research highlights the potential of waste foundry sand (WFS) as a partial substitute for flint-clay fines in silica–alumina refractory castables, delivering both environmental and cost benefits. With its high quartz content and fine granulometry, WFS is particularly compatible with refractory formulations. However, its use may increase water demand and porosity at intermediate firing stages, affecting microstructural integrity and mechanical performance. A key concern is the $\alpha \leftrightarrow \beta$ quartz transition near 573 °C, which can trigger microcracking upon cooling and compromise dimensional stability [25]. At higher temperatures, the reactive silica in WFS reacts with alumina from the matrix, promoting the crystallization of mullite. Mullite's interlocking, needle-like morphology contributes to densification, reduced porosity, and improved thermal–mechanical stability. Careful adjustment of particle-size distribution and firing schedules is therefore essential to optimize performance in WFS-containing castables [26].

In comparison with advanced low- or ultra-low-cement castables—which often involve high binder costs, complex processing, and variable reliability—conventional castables incorporating WFS provide a more accessible and sustainable alternative. Foundry sands from investment casting may even contain preformed crystalline phases such as mullite, cristobalite, or zircon, enhancing their suitability for reuse after appropriate treatment [27]. Investigations with analogous secondary raw materials, such as precision casting sands, indicate that partial replacements of ~10 wt.% can yield denser refractories with lower open porosity than virgin formulations. Nonetheless, residual binders and trace impurities in WFS require careful evaluation of phase evolution, leaching potential, and long-term durability under repeated thermal cycling [28].

The application of metallurgical slags as aggregates in refractory castables has received comparatively limited attention in the literature [29–32]. Nevertheless, several studies highlight their potential as sustainable secondary resources in high-temperature materials.

In 2018, Chargui et al. investigated mullite synthesis for refractory applications using stoichiometric mixtures of two natural kaolin types combined with aluminum slag. Their findings showed that mullite content increased progressively with firing temperature, and the resulting mullite exhibited a bimodal morphology: primary mullite generated by metakaolin disintegration at ~990 °C, and secondary mullite formed through a dissolution–precipitation mechanism from the glassy phase enriched with alumina from slag. This dual

mullite formation mechanism enhanced both crystallinity and microstructural stability, underscoring the viability of alumina-bearing slags as mullite precursors [33].

Similarly, in 2014 Kumar et al. produced conventional and low-cement castables using calcined bauxite, ferrochrome slag, and microsilica. Their formulations incorporated up to 50 wt.% ferrochrome slag across coarse, medium, and fine fractions, while microsilica (0–10 wt.%) partially substituted high-alumina cement (reducing cement content to 3–5 wt.%). The resulting castables demonstrated promising physical, mechanical, and thermal properties, confirming that ferrochrome slag can function effectively as a structural aggregate in both conventional and low-cement systems [33–35].

These studies collectively indicate that metallurgical slags—long regarded as waste streams—can serve as functional raw materials in refractory castables, enabling reductions in virgin resource demand, embodied energy, and overall production costs. However, further systematic research is required to address slag variability, residual contaminants, and long-term durability under service conditions. Blast furnace slag, due to its high CaO content, reacts with SiO_2 and Al_2O_3 during firing to form calcium aluminosilicate phases, primarily anorthite ($CaAl_2Si_2O_8$). The formation of anorthite is thermodynamically favored at elevated temperatures and can significantly influence the microstructural evolution of refractory castables. On one hand, anorthite enhances densification by filling intergranular pores and reinforcing grain boundaries, which translates into improved mechanical strength and thermal stability at moderate service temperatures. On the other hand, its stability window is limited: anorthite melts congruently at 1553 °C, making it less desirable for applications where refractories are exposed to higher operational temperatures or aggressive slag environments [36].

By contrast, mullite ($3Al_2O_3 \cdot 2SiO_2$) remains stable well above 1600 °C and is widely recognized as the backbone phase for high-performance aluminosilicate refractories due to its low thermal expansion, high creep resistance, and excellent thermal shock behavior. In slag-containing formulations, the interplay between mullite and anorthite becomes critical. Optimizing the balance between these phases allows for tailoring castables to specific applications: slag additions may promote anorthite formation, which is advantageous for intermediate-temperature systems such as biomass boilers (<1100–1300 °C), while mullite-dominated matrices are essential for steelmaking or cement kilns where service temperatures exceed 1500 °C.

Therefore, the careful design of firing schedules, raw material ratios, and slag incorporation strategies is necessary to control the relative amounts of anorthite and mullite. This balance ensures both cost efficiency and reliable long-term performance, aligning slag valorization with circular economy principles and cleaner production pathways in high-temperature industries.

On the other hand, population growth, industrialization, and urban expansion have accelerated both the demand for construction and infrastructure and the generation of industrial waste [37–39]. One sector particularly affected by these trends is the electrical power industry, which has experienced substantial expansion to meet rising electricity needs [23,40]. Since the mid-19th century, porcelain has been the dominant material for electrical insulators, valued for its mechanical strength, dielectric performance, and resistance to weathering [41–47]. Being the most popular electrical insulator, siliceous porcelain insulators are typically composed of 40–50 wt.% clay, 10–15 wt.% quartz, and 35–45 wt.% feldspar [48–54].

China is currently the largest producer, manufacturing over 1.8 million units annually as of 2017, with a projected 16% growth by 2022 [55]. However, the rapid expansion of this industry has also led to the accumulation of substantial amounts of porcelain waste—

generated both during manufacturing (due to quality control rejections) and at the end of service life.

Despite representing only about 5% of the capital cost of a transmission line, insulators account for up to 70% of outage-related expenses and around 50% of maintenance costs. Their average service life is approximately a decade [56], after which they require replacement. In Brazil alone, an estimated 25,000 tons of obsolete porcelain insulators are discarded annually, most ending up in landfills or illegal dumpsites, posing environmental and logistical challenges [57,58].

From a materials perspective, these discarded insulators are a potentially valuable secondary raw material. Their fired ceramic bodies—commonly referred to as chamotte—are rich in mullite and quartz phases, formed through high-temperature sintering (≈1200 °C) that reduces water absorption and enhances mechanical strength [59]. Previous research has explored the valorization of discarded porcelain insulators from the electrical industry as supplementary cementitious materials (SCMs) or as aggregates in Portland cement-based composites. These investigations have demonstrated that finely ground porcelain waste exhibits pozzolanic reactivity, enabling the formation of additional calcium silicate hydrate (C–S–H) phases during cement hydration. This reaction contributes to improved mechanical strength, reduced porosity, and enhanced long-term durability of the resulting materials [60–63]. Such findings highlight the potential of porcelain insulator waste as a viable, sustainable alternative to conventional raw materials, supporting circular economy strategies and reducing the environmental footprint of the cement and construction sectors. Although the reuse of porcelain waste in refractory applications remains underexplored, isolated studies have reported promising results. For instance, Xu et al. (2015) demonstrated that crushed electrical insulator waste could serve as aggregates in lightweight porous castables, improving thermal insulation performance [64].

Building on this concept, the present study proposes the partial replacement of flint clay with chamotte waste from rejected electrical porcelain insulators in the formulation of aluminosilicate refractory castables. The objective is to evaluate the effect of this substitution (5 and 10 wt.%) on the physico-mechanical performance and microstructural evolution of the castables across different firing temperatures. This approach aligns with sustainable manufacturing principles by promoting the circular use of industrial ceramics, reducing dependence on virgin minerals, and diverting high-volume waste from landfills—thereby contributing to both resource conservation and waste valorization in the refractory industry.

2. Experimental Procedure

2.1. Raw Materials

A conventional aluminosilicate refractory castable was designed using industrially relevant raw materials supplied by AP Green (Salinas Victoria, Nuevo León, Mexico). The formulation included calcined flint clay, calcined Guayanese bauxite, kyanite (48% Al_2O_3), calcium aluminate cement (Secar 80), and microsilica. Flint clay is a dense refractory raw material composed mainly of silica (~50 wt.% SiO_2) and alumina (~45 wt.% Al_2O_3), with minor Fe_2O_3 and trace alkali oxides. Its compact structure, conchoidal fracture, and high hardness impart excellent resistance to abrasion, corrosion, and thermal shock. In refractory castables, flint clay functions as a high-quality aggregate, ensuring structural integrity and durability under severe thermal and chemical environments. Guyanese bauxite, widely recognized for its superior quality, typically contains ≥88 wt.% Al_2O_3, ≤6 wt.% SiO_2, and ~1 wt.% Fe_2O_3, although composition varies among deposits. Its low impurity levels make it an optimal source of reactive alumina, promoting high refractoriness and stable mullite formation. Kyanite (−48 mesh), an aluminosilicate mineral (Al_2SiO_5), is valued for its elongated crystals that enhance strength and thermal shock resistance. Upon heating,

kyanite undergoes polymorphic transformation into mullite accompanied by ~15–18% volume expansion, effectively counterbalancing clay shrinkage and improving dimensional stability. Secar 80, a high-purity calcium aluminate cement (~80 wt.% Al_2O_3), exhibits controlled mineralogy with negligible free lime and crystalline silica. It offers rapid strength development, high refractoriness, and chemical resistance, enabling its widespread use as a binder in advanced refractory formulations. Microsilica, a by-product rich in amorphous SiO_2 with sub-micron spherical particles, enhances particle packing and reduces water demand in castables. Its high pozzolanic reactivity promotes in situ mullite formation or secondary bonding phases, thereby densifying the microstructure, reducing porosity, and improving both mechanical strength and high-temperature durability. Additionally, its valorization from industrial waste streams aligns with circular economy strategies.

To improve the environmental performance of the mix design, finely ground chamotte (<75 µm, obtained by mechanical sieving) was incorporated as a secondary raw material. Chamotte derived from quality rejected electrical porcelain insulators represents a calcined ceramic rich in alumina (Al_2O_3) and silica (SiO_2), which can be effectively reused as aggregate in refractory castables. Its dominant crystalline phases—mullite and cristobalite—confer high refractoriness, mechanical strength, and volumetric stability under severe thermal cycling. The presence of mullite contributes an interlocking microstructure that enhances flexural and compressive strength, while cristobalite assists in accommodating thermal stresses through controlled expansion. When incorporated into castable formulations, recycled chamotte improves thermal shock resistance and densification behavior, while maintaining dimensional stability at elevated temperatures. Beyond performance, its valorization reduces dependence on virgin raw materials, diverts ceramic waste from landfills, and lowers the environmental footprint of refractory production. These features position chamotte not only as a technically reliable aggregate but also as a sustainable substitute that supports circular economy pathways and cleaner production strategies in high-temperature industries. This chamotte, supplied by Celeco (Apodaca, Nuevo León, Mexico), was selected due to its potential to valorize ceramic waste streams while reducing the consumption of virgin refractory inputs.

The chemical composition of all raw materials, including chamotte, was determined via X-ray fluorescence (XRF) using a Panalytical MagiX PW2424 X-ray Fluorescence (XRF) Spectrometer (Philips, Malvern Panalytical, UK). Results are summarized in Table 2.

Table 2. Chemical composition of the raw materials used in the refractory castable (wt.%).

Oxide	Raw Materials (wt.%)					
	Secar 80	Microsilica	Flint Clay	Bauxite	Kyanite	Chamotte
SiO_2	0.40	94.33	47.85	9.18	41.20	69.56
Al_2O_3	78.76	0.78	43.59	81.17	54.73	21.37
Fe_2O_3	0.61	1.04	2.23	4.93	1.47	1.63
CaO	17.80	0.72	0.14	0.12	0.11	0.49
MgO	0.17	0.61	0.22	0.00	0.00	0.26
SO_3	0.04	0.18	0.04	0.01	0.15	0.03
Na_2O	1.26	0.19	0.00	0.00	0.08	2.58
K_2O	0.00	0.49	0.65	0.00	0.00	2.14
P_2O_5	0.11	0.07	0.20	0.09	0.14	0.16
Cr_2O_3	0.18	0.04	0.28	0.66	0.20	0.18
Mn_2O_3	0.00	0.10	0.00	0.04	0.00	0.00
TiO_2	0.00	0.00	2.40	3.29	1.46	0.87
ZrO_2	0.00	0.00	0.13	0.29	0.05	0.17
L.O.I.	0.67	1.45	2.27	0.22	0.41	0.56
Total	100.0	100.0	100.0	100.0	100.0	100.0

Phase assemblages were identified by X-ray diffraction (XRD) employing a Panalytical Empyrean diffractometer (Malvern Panalytical, UK) equipped with Cu-Kα radiation (λ = 1.5406 Å), operating at 45 kV and 40 mA. Diffraction data were collected under identical conditions: a 2θ range of 10–100°, using a θ/2θ scan mode, with a step size of 0.013° and a counting time of 10 s per step. Measurements were performed at the Centro de Investigación e Innovación en Ingeniería Aeronáutica (CIIIA-UANL, Nuevo León, Mexico).

The diffraction patterns, that will be discussed in the Results Section, provided detailed insights into the crystalline phases and residual amorphous constituents of the raw materials. This characterization was essential for understanding their reactivity and contribution to the microstructural evolution of the refractory castable.

Method of Recycling Porcelain Scrap

Porcelain insulators rejected by quality control were selected as the source material to produce chamotte powders for this study, valorizing ceramic waste within a sustainable raw material framework. Large insulator fragments (~75 mm) were initially comminuted in a Jaw crusher (McLanahan, Model 4R-6, Hollidaysburg, Pennsylvania, USA) yielding pieces between 30 and 40 mm. A subsequent stage of crushing with a Jaw crusher (Bico, Model LC-33, Burbank, California, USA) reduced the fragments to ~10 mm. The material was then processed in a Pulverizer (Bico, Model UA, Burbank, California, USA), generating coarse chamotte sand in the range of 3–5 mm. To obtain finer scrap powders (<75 μm), the product was further milled using a Vibro-Energy grinding mill (Sweco, Model DM1, Florence, KY) with alumina ball media, ensuring minimal contamination from wear. Finally, magnetic separation was employed to eliminate residual iron impurities, thereby improving chemical purity and consistency of the recycled material.

The resulting chamotte exhibited a median particle size of 26 μm, as determined with a laser diffraction particle size analyzer (Microtrac S3500, Microtrac Inc., York, Pennsylvania, USA). This particle size distribution is suitable for optimizing packing density and reactivity in refractory castable formulations, while also demonstrating that porcelain waste can be efficiently transformed into high-quality raw materials for sustainable high-temperature applications.

2.2. Refractory Formulation and Specimen Preparation

A reference composition (control) was prepared using calcined flint clay, bauxite, kyanite (48% Al_2O_3), calcium aluminate cement (Secar 80), and microsilica. To explore sustainable alternatives, two additional formulations were designed in which the fine fraction of flint clay was partially replaced with 5 and 10 wt.% chamotte, respectively. This substitution aimed to evaluate the feasibility of chamotte waste as a secondary raw material for eco-efficient refractory castables.

The complete mixture design, including aggregate and binder contents, particle size distribution, and required water addition, is summarized in Table 3. For clarity, the mixtures are designated as: CC-Control castable (commercial reference); 5CH-Castable with 5 wt.% chamotte; 10CH-Castable with 10 wt.% chamotte.

Each formulation was homogenized in a laboratory mortar mixer (model Mortar Grinder RM 200, Retsch, Germany). Dry blending was performed for 3 min to ensure uniform dispersion of powders, followed by the addition of ~11 wt.% clean water, in accordance with ASTM C860 [65], to achieve proper consistency and workability. Wet mixing continued for an additional 4 min. The resulting pastes were poured into pre-lubricated acrylic molds, previously coated with a thin film of mineral oil (commercial Vaseline) to facilitate demolding. Specimens with dimensions of 50 × 50 × 50 mm^3 were

prepared for compressive strength testing, while 25 × 25 × 150 mm^3 prisms were cast for flexural strength evaluation.

Table 3. Batch composition of conventional and sustainable refractory castables (wt.%).

Raw Material	Grain Size	Control	5CH wt.%	10CH
Flint clay	(6.3–4 mm)	5.0	5.0	5.0
	(4–2 mm)	10.0	10.0	10.0
	(<2 mm)	5.0	5.0	5.0
	Fine (MB)	20	15	10
Bauxite	(4–2 mm)	10.0	10.0	10.0
	(<2 mm)	10.0	10.0	10.0
	Fine (MB)	20.0	20.0	20.0
Secar 80	(<75 µm)	12.5	12.5	12.5
Kyanite	(<75 µm)	5.0	5.0	5.0
Microsilica	(<75 µm)	2.5	2.5	2.5
Chamotte	(<75 µm)	0.0	5.0	10.0
Mixing water	–	11.0	11.25	11.5

During casting, vibration was applied for 3 min on a CONTROLS 55-C0160/Hz vibrating table (CONTROLS, Milan, Italy) to remove entrapped air. Molds were sealed with plastic film to minimize moisture loss and stored at laboratory conditions for 24 h. Subsequently, the specimens were demolded and oven-dried at 110 °C for 24 h in a Thermo Scientific Heratherm unit (Thermo Fisher Scientific, Waltham, Massachusetts, USA). Heat treatments were then carried out at 815, 1050, and 1400 °C using a Thermo Scientific Lindberg Blue M/1700 electric furnace (Thermo Fisher Scientific, Waltham, Massachusetts, USA). The heating rate was fixed at 170 °C/h with a soaking time of 4 h at each target temperature, followed by furnace cooling to ambient conditions, in accordance with ASTM C865 [66].

The 110–120 °C drying step is not a sintering stage, but rather a controlled removal of physically bound water and residual moisture from the castables. At this temperature, free water evaporates, and the chemically adsorbed water in hydrated cementitious phases begins to release gradually, without inducing cracking. This step ensures dimensional stability before higher-temperature treatments, minimizes explosive spalling, and standardizes the baseline condition of the specimens for further testing. ASTM C865 also prescribes drying at ~110 °C as a reference condition for measuring properties such as density, porosity, and strength in refractory castables.

The temperatures 815 °C, 1050 °C, and 1400 °C corresponds to a critical stage in phase development and performance evaluation of aluminosilicate refractory castables. Around ≈815 °C (often rounded as 850 °C in practice), dehydroxylation of kaolinite → metakaolinite occurs. Minor phase rearrangements, shrinkage, and the first glassy phases can develop. In cement-bonded castables, calcium aluminate hydrates (CAH, C_2AH_8, C_3AH_6) fully decompose, leaving transitional aluminas and an initial porous skeleton. This step is critical to study dimensional stability, onset of strength loss, and microstructural changes under moderate heat exposure. 1050 °C is a transitional firing level, where metakaolinite transforms into spinel-type phases and silica-rich glass. At this temperature, initial formation of primary mullite begins. This stage is chosen to track how early mullitization and densification improve mechanical performance, especially modulus of rupture and resistance to thermal shock. It also simulates medium-temperature service

conditions, such as in biomass boilers or ceramic furnaces. 1400 °C is the high-temperature consolidation stage. At this temperature, full development of secondary mullite (needle-like crystals) and anorthite (from $CaO–Al_2O_3–SiO_2$ reactions) occurs. At this level, the microstructure reaches maximum densification, strength, and thermal stability. Evaluating properties at 1400 °C simulates severe industrial service conditions (slag contact, alkali attack, high mechanical load).

This systematic preparation route ensured consistent processing conditions, enabling reliable assessment of the influence of chamotte substitution on the physical and mechanical performance of the refractory castables.

2.3. Characterization Techniques

2.3.1. Physical Properties

Bulk density and apparent porosity were determined at each firing temperature by the boiling water method combined with Archimedes' principle, in accordance with ASTM C20 [67]. For each condition, six specimens were tested, and results are reported as mean values with corresponding standard deviations to ensure statistical reliability.

2.3.2. Mechanical Properties

The cold crushing strength (CCS) and flexural strength were measured to assess the mechanical performance of the castables. Tests were carried out using an ELE-International hydraulic universal testing machine (ELE International, Manchester, UK), with a maximum capacity of 250 kN. Cubic samples were loaded at a constant rate of 31.2 kN/min for CCS determination, while flexural strength was measured by three-point bending on prism specimens at a loading rate of 0.774 kN/min, following ASTM C133 [68]. Each reported value corresponds to the average of six replicates, with standard deviations included.

2.3.3. Crystalline Phase Evolution of Secar 80 Cement and Kyanite

The crystalline phase evolution of Secar 80 cement and kyanite was investigated by in situ high-temperature X-ray diffraction (HT-XRD). Diffractograms were collected at selected temperatures ranging from 110 to 1500 °C: 110, 280, 520, 680, 960, 1270, and 1350 °C for Secar 80, and 150, 580, 900, 1250, 1330, 1430, and 1500 °C for kyanite. Measurements were performed in the 10–140° 2θ range with a step size of 0.01313° and 10 s counting time per step, using a Panalytical Empyrean diffractometer (Panalytical, Almelo, Netherlands) with Cu-Kα radiation, equipped with a Bragg–Brentano goniometer and an Anton Paar HTK 16N platinum-strip furnace chamber (Anton Paar GmbH, Graz, Austria). For the formulated castables, phase identification was performed by room-temperature XRD (Panalytical Empyrean, Cu-Kα radiation, λ = 1.5406 Å, 45 kV, 40 mA). Patterns were collected in the angular range 20–100° (2θ) using a θ–2θ configuration, with a step width of 0.0167° and a counting time of 80 s per step. Crystalline phases were identified using reference patterns from the Crystallographic Open Database (COD).

2.3.4. TGA/SDTA Measurements

The thermal evolution of Secar 80 cement and Kynite were determined by thermogravimetric (TGA) and differential thermal analysis (SDTA) analysis. The thermal analysis was performed in flowing air (total flow air rate: 40 mL/min) at a heating rate of 5 °C/min from room temperature to 1500 °C placing 35 mg of sample weight and analyzing in a Mettler-Toledo TGA/SDTA 851e Thermo-Analyser (Columbus, OH, USA). For thermal measurements, the tested samples in the form of powder were placed in an Al_2O_3 crucible type. The weight of the samples was determined using the CPA analytical balance (Sartorius, Göttingen, Germany). All obtained thermal curves were analyzed using Proteus 8.0 software produced by Netzsch company (Gebrüder-Netzsch-Straße, Germany).

2.3.5. Microstructural Analysis

Microstructural features of the specimens sintered at 1400 °C were examined by scanning electron microscopy SEM (JEOL JSM-6510LV) (JEOL, Tokyo, Japan), equipped with an EDAX Apollo X EDS system (EDAX Inc., Mahwah, NJ, USA).

Prior to analysis, samples were cold-mounted in epoxy resin and sequentially polished using silicon carbide abrasive papers (grits 80–4000) followed by diamond suspensions (9, 3, and 1 µm). The polished surfaces were coated with a thin layer of gold using a Quorum Q150R ES sputter coater (Quorum Technologies Ltd., East Sussex, UK) to ensure adequate conductivity during imaging.

3. Results and Discussion

3.1. Characterization of Raw Materials and Chamotte

Table 4 shows the crystalline phases of the raw materials employed, including chamotte. In the case of chamotte, the main reflections correspond to quartz (SiO_2, ICDD 01-087-2096) and mullite ($Al_{2.272}Si_{0.728}O_{4.864}$, ICDD 01-083-1881), which are well-known constituents in alumino-silicate refractories. These two phases are highly desirable in refractory formulations due to their combined effect of mechanical robustness, thermal stability, and relatively low thermal conductivity [69,70]. Mullite, in particular, is regarded as the most stable phase in the Al_2O_3–SiO_2 system and significantly contributes to the resistance of refractories under severe thermal cycling. Its development is strongly dependent on the Al_2O_3/SiO_2 ratio and can be promoted through the inclusion of reactive silica sources such as microsilica, which enhances sintering and densification, leading to lower porosity and higher hot strength [71,72].

Table 4. Crystalline phases of the raw materials employed in the design of refractory castables.

	Raw Materials				
	Chamotte	**Calcined Flint Clay**	**Calcined Bauxite**	**Kyanite**	**Secar 80**
Crystalline Phases	Quartz (SiO_2) ICDD 01-087-2096	Mullite ($Al_{2.272}Si_{0.728}O_{4.864}$) ICDD 01-083-1881	Corundum (α-Al_2O_3) ICDD 01-070-7049	Kyanite (Al_2SiO_5) ICDD 01-072-1447	Calcium monoaluminate (CA) ICDD 01-076-7124
	Mullite ($Al_{2.272}Si_{0.728}O_{4.864}$) ICDD 01-083-1881	Cristobalite (SiO_2) ICDD 01-087-2096	Mullite ($Al_{2.272}Si_{0.728}O_{4.864}$) ICDD 01-083-1881	Quartz (SiO_2) ICDD 01-087-2096	Calcium dialuminate (CA_2) ICDD 01-089-3851
		Rutile (TiO_2) ICDD 01-087-2096	Aluminum titanate (Al_2TiO_5) ICDD 01-076-8797	Rutile (TiO_2) ICDD 01-087-2096	Corundum (α-Al_2O_3) ICDD 01-070-7049
			Quartz (SiO_2) ICDD 01-087-2096		

Calcined flint clay exhibited mullite ($Al_{2.272}Si_{0.728}O_{4.864}$, ICDD 01-083-1881) and cristobalite (SiO_2, ICDD 01-087-2096) as the dominant phases, with minor rutile- (TiO_2, ICDD 01-087-2096). Calcined bauxite, characterized by its high alumina content, contained corundum (α-Al_2O_3, ICDD 00-043-1484), mullite ($Al_{2.272}Si_{0.728}O_{4.864}$, ICDD 01-083-1881), aluminum titanate (Al_2TiO_5, ICDD 01-076-8797), and traces of quartz (SiO_2, ICDD 01-087-2096),

providing the system with high refractoriness and corrosion resistance. Kyanite, known as a precursor of mullite, displayed reflections of kyanite (Al_2SiO_5, ICDD 01-072-1447) itself together with quartz (SiO_2, ICDD 01-087-2096) and rutile (TiO_2, ICDD 01-087-2096), confirming its progressive transformation into mullite and cristobalite upon heating, a process that contributes to volume stability at elevated temperatures.

The calcium aluminate cement-Secar 80 presented crystalline phases of calcium monoaluminate (CA, ICDD 01-076-7124), calcium dialuminate (CA_2, ICDD 01-089-3851), and corundum (α-Al_2O_3, ICDD 01-070-7049). These phases are responsible for the hydraulic reactivity at ambient conditions, providing early mechanical strength and serving as a bonding matrix prior to high-temperature firing. Finally, microsilica displayed the characteristic broad amorphous halo of silica, which highlights its role as a reactive pozzolanic additive. Beyond improving packing density, the amorphous silica facilitates the formation of secondary mullite during sintering, thereby contributing to improved bonding, reduced porosity, and enhanced high-temperature performance of the refractory composites.

3.2. Crystalline Phase Analysis of Refractory Specimens

3.2.1. Control Composition (CC)

Figure 1 presents the XRD patterns of the control composition (CC) refractory specimen at different firing temperatures. At 110 °C, the diffractogram revealed mullite ($Al_{2.272}Si_{0.728}O_{4.864}$, ICDD 01-083-1881), corundum (α-Al_2O_3, ICDD 01-088-0826), kyanite (Al_2SiO_5, ICDD 01-072-1447), cristobalite (SiO_2, ICDD 01-082-0512), rutile (TiO_2, ICDD 03-065-1119), and gibbsite (γ-$Al(OH)_3$, ICDD 01-076-1782) as the main crystalline constituents. The gibbsite phase originates from the hydration products of calcium aluminate cement (CAC). When heated to 815 °C, the characteristic gibbsite reflection at $2\theta \approx 18.3°$ disappeared, indicating dehydroxylation and the breakdown of hydrated alumina species. In this temperature range, mullite, corundum, cristobalite, and kyanite peaks showed no significant variation in intensity, confirming their thermal stability. Mullite and cristobalite are widely reported to be stable well beyond 1200 °C, with mullite growth becoming more pronounced at elevated temperatures, while corundum maintains stability even under repeated thermal shocks [73–75].

Kyanite, though metastable at higher temperatures, remains unaltered up to approximately 1050 °C under ambient pressure [76]. Between 815 °C and 1050 °C, no major phase changes were detected, and the crystalline framework was essentially preserved. Literature confirms that kyanite does not undergo abrupt structural transformations in this interval, exhibiting only gradual lattice adjustments such as minor changes in vibrational modes and unit cell parameters [77,78]. Its transformation to mullite and silica typically requires firing above 1200 °C or high-pressure conditions [79]. At 1400 °C, significant mineralogical changes were observed. Kyanite reflections disappeared, while new peaks corresponding to anorthite ($CaAl_2Si_2O_8$, ICDD 01-070-0287) emerged. The decomposition of kyanite into mullite and free silica is well-documented in this temperature window [75], and the crystallization of anorthite is attributed to the interaction of CaO—released from CAC decomposition or present as minor impurities—with silica-rich glassy phases formed above 1000 °C [80–82]. This process is consistent with phase equilibria reported for calcium-bearing aluminosilicate systems. The coexistence of mullite and anorthite has practical implications for refractory performance. While mullite provides excellent refractoriness, creep resistance, and thermal stability, controlled amounts of anorthite may improve mechanical strength and toughness by refining the microstructure [80,81]. However, excessive anorthite formation can be detrimental, lowering refractoriness due to its relatively lower melting temperature compared with mullite [80].

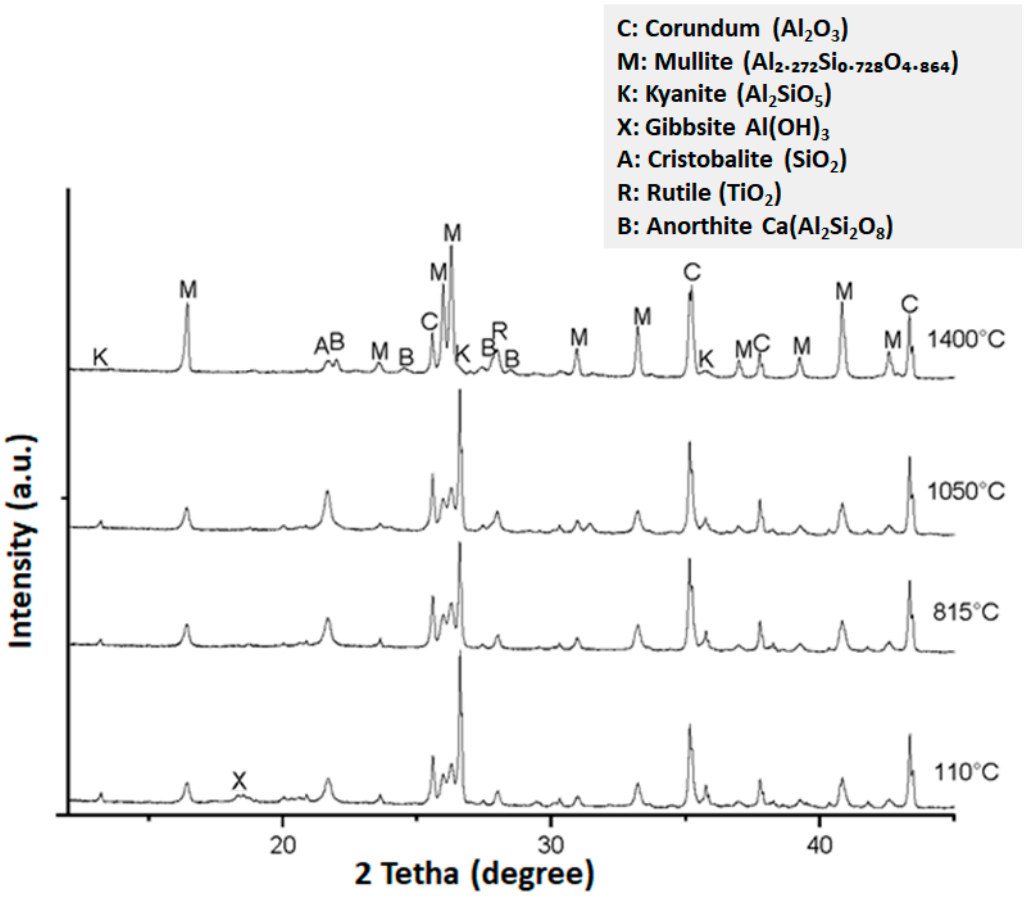

Figure 1. Comparative XRD patterns of the Control composition at 110, 815, 1050, and 1400 °C. C = Corundum (α-Al_2O_3); M = Mullite ($Al_{2.272}Si_{0.728}O_{4.864}$); K = Kyanite ($Al_2SiO_5$); X = Gibbsite ($Al(OH)_3$); A = Cristobalite ($SiO_2$); R = Rutile ($TiO_2$); B = Anorthite ($Ca(Al_2Si_2O_8)$).

As observed, the control formulation displayed progressive enrichment in mullite with increasing temperature, confirming its dominant role in conferring refractory properties. The emergence of anorthite at 1400 °C reflects fluxing effects of CaO from CAC and minor impurities, which promote liquid phase formation and influence the final microstructural development.

3.2.2. 5CH Composition

Figure 2 presents the XRD patterns of the chamotte-containing refractory specimen (5CH) after firing at 110, 815, 1050, and 1400 °C. At 110 °C, the detected phases include mullite ($Al_{2.272}Si_{0.728}O_{4.864}$, ICDD 01-083-1881), corundum (α-Al_2O_3, ICDD 01-088-0826), kyanite (Al_2SiO_5, ICDD 01-072-1447), cristobalite (SiO_2, ICDD 01-082-0512), rutile (TiO_2, ICDD 03-065-1119), and gibbsite ($Al(OH)_3$, ICDD 01-076-1782). Upon heating to 815 °C, gibbsite reflections (notably at $2\theta \approx 18.3°$) vanish due to dehydration, while mullite, corundum, kyanite, cristobalite, and rutile remain stable up to ~900 °C, consistent with the expected thermal stability of aluminosilicate refractories [82–84]. Rutile is likely derived from the anatase-to-rutile transformation, a well-documented transition under these conditions [84]. Between 815 °C and 1050 °C, no significant qualitative changes were observed, indicating a relatively stable crystalline assemblage. In contrast, heating from 1050 °C to 1400 °C promoted pronounced phase transformations. Kyanite reflections completely disappeared, accompanied by a marked increase in the intensity of mullite peaks (particularly at $2\theta \approx 25.98°$ and 26.28°), confirming the progressive conversion of kyanite into secondary mullite. This transformation, generally occurring between 1350 and 1400 °C, involves

the breakdown of kyanite with the concurrent crystallization and coarsening of mullite grains, which tend to evolve from acicular morphologies to more equiaxed or platelet-like structures at higher temperatures [74,85]. At 1400 °C, new reflections corresponding to anorthite ($CaAl_2Si_2O_8$, ICDD 01-070-0287) were identified.

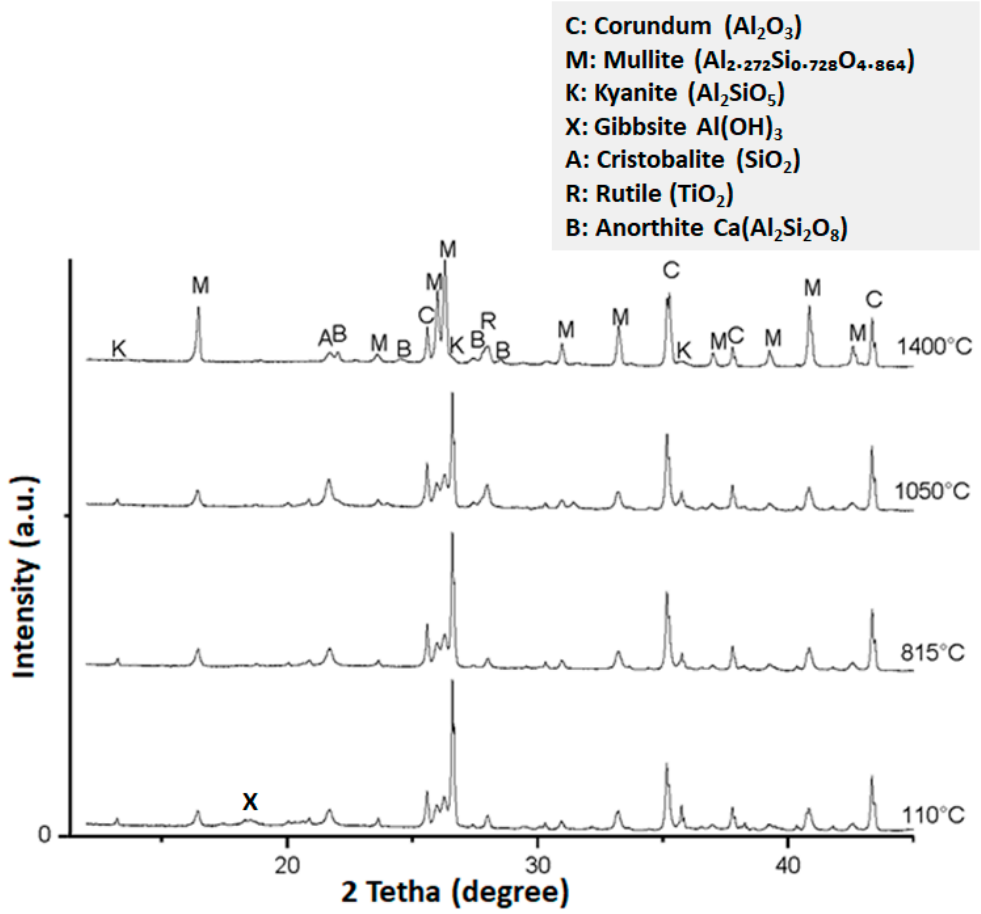

Figure 2. XRD patterns of the 5CH formulation after firing at 110, 815, 1050, and 1400 °C. Phase labels: C = Corundum (α-Al_2O_3); M = Mullite ($Al_{2.272}Si_{0.728}O_{4.864}$); K = Kyanite ($Al_2SiO_5$); X = Gibbsite ($Al(OH)_3$); A = Cristobalite ($SiO_2$); R = Rutile ($TiO_2$); B = Anorthite ($CaAl_2Si_2O_8$).

This phase originates from reactions among CaO, SiO_2, and Al_2O_3, facilitated by the presence of calcium aluminate cement in the formulation. The coexistence of mullite and anorthite is frequently observed in CaO-containing refractory systems and can enhance mechanical performance when appropriately distributed in the microstructure. Specifically, the formation of a mullite–anorthite composite matrix has been linked to increased bending strength and thermal shock resistance, provided that excessive liquid-phase generation is avoided [80,86].

The sequence of main reactions explaining these transformations can be summarized as follows:

$$2\ Al(OH)_3 \rightarrow Al_2O_3 + 3\ H_2O \text{ (gibbsite dehydration, <300 °C)} \quad (1)$$

$$3\ Al_2SiO_5 \rightarrow 3Al_2O_3{\cdot}2SiO_2 \text{ (mullite)} + SiO_2 \text{ (kyanite} \rightarrow \text{mullite + silica, 1350–1400 °C)} \quad (2)$$

$$CaO + Al_2O_3 + 2\ SiO_2 \rightarrow CaAl_2Si_2O_8 \text{ (anorthite) } (\geq 1350\ °C) \quad (3)$$

The principal mineralogical transformations occurring between 1050 and 1400 °C are summarized in Table 5. Literature reports also indicate that the mullite-to-anorthite ratio

plays a decisive role in tuning porosity, strength, and thermal conductivity, with mullite contributing to densification and high-temperature stability, whereas controlled amounts of anorthite can improve toughness and reduce microcracking [87,88].

Table 5. Phase transformations from kyanite to mullite and anorthite at high temperaturas.

Temperature Range	Main Phase Changes	Mechanism	Ref.
1050–1350 °C	Kyanite stable; mullite increases	Initial kyanite → mullite conversion begins	[86]
1350–1400 °C	Kyanite disappears; mullite grows	Complete kyanite → mullite transformation	[81]
∼1400 °C	Anorthite appears	CaO reacts with SiO_2 and Al_2O_3; anorthite forms	[75]

In summary, the phase evolution of the 5CH specimen is consistent with that of the control composition, demonstrating that the partial substitution of flint clay by 5 wt.% chamotte preserves the dominant crystalline phases across the investigated temperature range. The main differences lie in phase proportions at elevated temperatures, particularly in the extent of mullite crystallization and the late-stage formation of anorthite, both of which are critical for optimizing the performance of sustainable aluminosilicate castables.

3.2.3. 10CH Composition

Figure 3 presents the XRD patterns of the 10CH refractory specimen after firing at 110, 815, 1050, and 1400 °C. At 110 °C, the crystalline assemblage consisted of mullite ($Al_{2.272}Si_{0.728}O_{4.864}$, ICDD 01-083-1881), corundum (α-Al_2O_3, ICDD 01-088-0826), kyanite (Al_2SiO_5, ICDD 01-072-1447), cristobalite (SiO_2, ICDD 01-082-0512), rutile (TiO_2, ICDD 03-065-1119), and gibbsite ($Al(OH)_3$, ICDD 01-076-1782). Upon heating to 815 °C, reflections associated with gibbsite (notably at $2\theta \approx 18$–$19°$) were no longer detected. This is consistent with its well-documented dehydroxylation pathway, which initiates near 220 °C and proceeds through a series of transitions—gibbsite → boehmite (γ-AlOOH) → transition aluminas (γ-, δ-, θ-Al_2O_3)—before stabilizing as α-Al_2O_3 at higher temperatures [89–91]. Thus, the absence of gibbsite peaks at 815 °C reflects the completion of hydroxyl group removal and the crystallization of alumina-rich intermediates. Other phases, namely mullite, corundum, kyanite, cristobalite, and rutile, remained unchanged, highlighting that gibbsite is the least thermally stable component in the initial mixture [92]. No significant qualitative phase modifications were observed at 1050 °C compared with the 815 °C diffractogram, suggesting a relative stability of the mullite–corundum–silica–rutile assemblage in this temperature interval. However, major transformations were detected after firing at 1400 °C. At this stage, kyanite reflections disappeared completely, accompanied by a marked increase in mullite peak intensities ($2\theta \approx 25.96°$ and $26.25°$), confirming the kyanite-to-mullite conversion that typically occurs in the 1350–1400 °C range. This transformation is relevant, as it contributes to the development of a dense mullite skeleton that enhances refractoriness and creep resistance [74,85]. Additionally, new reflections corresponding to anorthite ($CaAl_2Si_2O_8$, ICDD 01-070-0287) appeared at 1400 °C, resulting from solid-state reactions among CaO, SiO_2, and Al_2O_3.

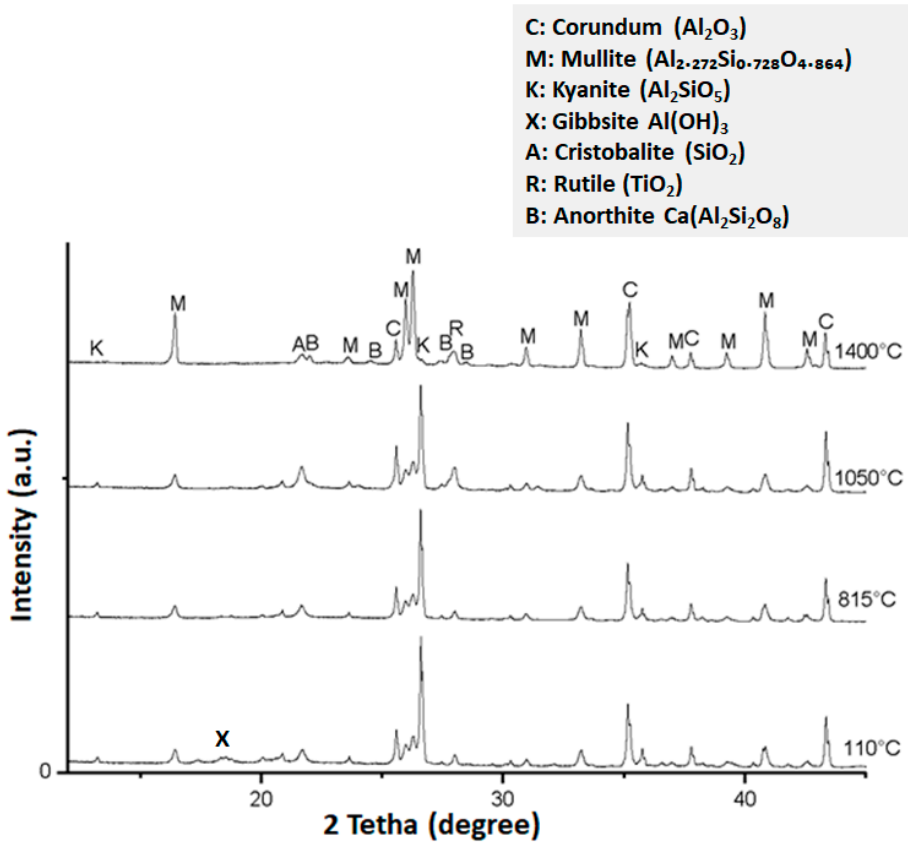

Figure 3. Comparative XRD patterns of the 10CH composition at 110, 815, 1050, and 1400 °C. Identified crystalline phases: C = Corundum (α-Al_2O_3); M = Mullite ($Al_{2.272}Si_{0.728}O_{4.864}$); K = Kyanite ($Al_2SiO_5$); X = Gibbsite ($Al(OH)_3$); A = Cristobalite ($SiO_2$); R = Rutile ($TiO_2$); and B = Anorthite ($CaAl_2Si_2O_8$).

The crystallization of anorthite is favored by the presence of calcium aluminate cement in the formulation, and its coexistence with mullite is characteristic of aluminosilicate refractories containing CaO [93]. When adequately distributed, anorthite can fill intergranular spaces, reduce residual porosity, and improve thermal shock resistance, although excessive amounts may generate liquid phases that compromise dimensional stability at service temperatures [80,86].

The thermal transformations observed in the 10CH refractory system can be represented as follows:

1. Dehydroxylation of gibbsite (220–350 °C):

$$2\ Al(OH)_3 \rightarrow \gamma\text{-}AlOOH\ (boehmite) + H_2O\ (g) \tag{4}$$

2. Formation of transition aluminas (350–1000 °C):

$$\gamma\text{-}AlOOH \rightarrow \gamma\text{-}Al_2O_3,\ \delta\text{-}Al_2O_3,\ \theta\text{-}Al_2O_3 \tag{5}$$

3. Stabilization of corundum (above ~1100 °C):

$$\theta\text{-}Al_2O_3 \rightarrow \alpha\text{-}Al_2O_3\ (corundum) \tag{6}$$

4. Kyanite decomposition and mullite crystallization (1350–1400 °C):

$$3\ Al_2SiO_5 \rightarrow 3Al_2O_3{\cdot}2SiO_2\ (mullite) + SiO_2\ (cristobalite) \tag{7}$$

5. Anorthite formation at high temperature (CaO-containing system):

$$CaO + Al_2O_3 + 2\,SiO_2 \rightarrow CaAl_2Si_2O_8 \text{ (anorthite)} \quad (8)$$

Overall, the mineralogical evolution of the 10CH composition closely mirrors that of the control and 5CH compositions, with the main differences being the relative proportions of mullite and anorthite formed at high temperature. These results indicate that the partial substitution of flint clay by 10 wt.% chamotte promotes the development of a mullite–anorthite composite matrix at 1400 °C. This combination is technologically advantageous, as mullite provides high-temperature stability and chemical resistance, while controlled amounts of anorthite enhance toughness and reduce microcracking. Therefore, the 10CH composition demonstrates potential for improved mechanical and thermo-mechanical performance when optimized at the microstructural level.

3.2.4. Rietveld Refinement Analysis

To complement the qualitative phase identification obtained from XRD, a Rietveld refinement was conducted on the samples sintered at 1400 °C for the three formulations (Control, 5CH, and 10CH). This quantitative approach allowed for a precise determination of crystalline phase proportions, thereby enabling a more reliable correlation between phase assemblage and the mechanical behavior of the refractories at high temperature.

The refinement results (Table 6) highlight a systematic evolution in phase composition with increasing chamotte substitution. Mullite content exhibited a progressive rise, reaching an increment of approximately +6.6 wt.% in the 10CH formulation compared to the control composition. In contrast, the relative fractions of anorthite and corundum decreased, while cristobalite showed only a marginal increase across the compositions.

Table 6. Rietveld refinement results of crystalline phases at 1400 °C for experimental compositions.

Sample	Phase	wt.%	Lattice Parameters (Å, °)	χ^2
Control	Mullite	57.8	a = 7.554, b = 7.696, c = 2.888, $\alpha = \beta$ = 90, γ = 90	2.27277
	Corundum	27.2	a = 4.761, b = 4.761, c = 12.996, $\alpha = \beta$ = 90, γ = 120	
	Anorthite	14.2	a = 8.173, b = 12.868, c = 12.927, α = 85.846, β = 81.042, γ = 89.190	
	Cristobalite	0.7	a = 4.997, b = 4.997, c = 7.07, $\alpha = \beta = \gamma$ = 90	
5CH	Mullite	58.2	a = 7.554, b = 7.696, c = 2.888, $\alpha = \beta$ = 90, γ = 90	2.23914
	Corundum	27.4	a = 4.761, b = 4.761, c = 12.996, $\alpha = \beta$ = 90, γ = 120	
	Anorthite	13.7	a = 8.173, b = 12.868, c = 12.925, α = 85.883, β = 81.065, γ = 89.184	
	Cristobalite	0.7	a = 4.997, b = 4.997, c = 7.07, $\alpha = \beta = \gamma$ = 90	
10CH	Mullite	61.6	a = 7.553, b = 7.695, c = 2.887, $\alpha = \beta$ = 90, γ = 90	2.26134
	Corundum	23.9	a = 4.761, b = 4.761, c = 12.996, $\alpha = \beta$ = 90, γ = 120	
	Anorthite	13.6	a = 8.173, b = 12.868, c = 12.925, α = 85.854, β = 81.075, γ = 89.296	
	Cristobalite	0.8	a = 4.997, b = 4.997, c = 7.07, $\alpha = \beta = \gamma$ = 90	

The enrichment in mullite is particularly relevant, as this phase is associated with a unique combination of properties including high refractoriness (mp = ~1810 °C to 1850 °C), low thermal expansion coefficient (~5 × 10^{-6} K^{-1}), and excellent resistance to mechanical and thermal shock. This finding suggests that the incorporation of chamotte fosters mullite crystallization, likely by enhancing the reactive interface between silica and alumina-rich phases at elevated temperatures.

The reduced presence of corundum and anorthite in chamotte-containing samples may be attributed to competitive phase formation, where alumina preferentially reacts with silica from chamotte to stabilize mullite, thereby limiting the availability of Al_2O_3 for corundum crystallization and Ca–Al–Si interactions for anorthite development. This mineralogical redistribution supports the mechanical performance improvements observed in the optimized compositions.

It is important to recognize, however, that these variations cannot be solely ascribed to phase equilibria. Additional factors—including differences in particle size distribution, reactivity of raw materials, and the presence of minor oxides from chamotte—may also play a role in modulating phase assemblage.

3.3. Thermal Evolution of Secar 80 and Kyanite

The thermal stability of Secar 80, employed as a calcium aluminate cement (CAC) binder, and kyanite, used as a mullite precursor, was investigated by thermogravimetric analysis (TGA), differential thermal analysis (SDTA), and in situ high-temperature X-ray diffraction (HT-XRD). The measurements were carried out up to 1500 °C using an Anton Paar HTK 16N chamber, enabling a detailed evaluation of crystallographic transformations during heating. This combined approach allowed us to correlate weight loss and endothermic events with the progressive development of high-temperature phases relevant to refractory performance.

3.3.1. Thermal Analysis (TGA–SDTA) of Secar 80 and Kyanite

The TGA– SDTA curves are presented in Figures 4 and 5, where Figure 4 corresponds to Secar 80 and Figure 5 to kyanite.

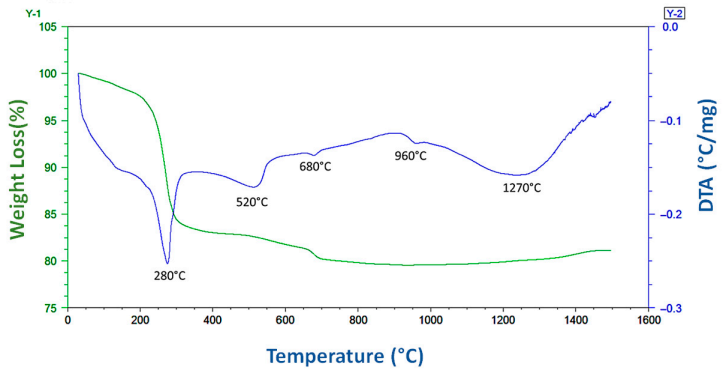

Figure 4. TGA–SDTA curves of Secar 80, showing characteristic thermal events and mass loss steps used to determine the target temperatures for HT–XRD analysis.

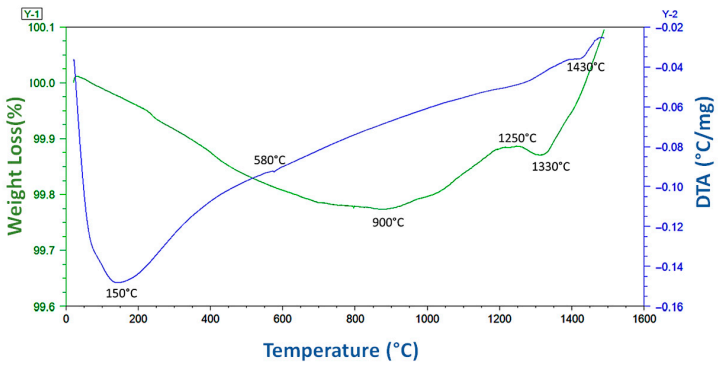

Figure 5. TGA–SDTA curves of Kyanite, showing characteristic thermal events and mass loss steps used to determine the target temperatures for HT–XRD analysis.

For Secar 80 (Figure 4), eight characteristic temperatures (25, 110, 280, 520, 680, 960, 1270, and 1350 °C) were selected for subsequent HT-XRD analysis. Five distinct endothermic peaks were detected at 280, 520, 680, 960, and 1270 °C, corresponding to stepwise decomposition of hydration products and subsequent phase stabilization. Between 280 °C and 680 °C, gibbsite ($Al(OH)_3$) and hydrated calcium aluminates (e.g., $Ca_3Al_2O_6{\cdot}6H_2O$ and C_3AH_6) undergo progressive dehydration, producing a substantial mass loss (~20%) and leading to the crystallization of mayenite ($C_{12}A_7$) and corundum (Al_2O_3). This agrees with previous observations that the breakdown of hydrated aluminates drives the stabilization of CA_2 and Al_2O_3 at intermediate temperatures [94]. At higher temperatures, specifically above 960 °C, further endothermic signals correspond to the destabilization of anhydrous aluminates (CA and CA_2), accompanied by additional corundum formation. The final peak at 1270 °C reflects advanced decomposition, a transformation highly relevant for CAC-based refractory systems because it dictates the balance between transient phases ($C_{12}A_7$, CA_2) and stable high-temperature assemblages (Al_2O_3, mullite). These changes directly affect chemical stability and hot mechanical performance [95,96].

For kyanite (Figure 5), three principal endothermic peaks were identified at 150, 580, and 1430 °C, alongside two minor weight losses at 900 °C (0.33%) and 1330 °C (0.02%). The initial event at 150 °C corresponds to the release of surface-adsorbed water, with no major crystallographic modification. Between 580 °C and 900 °C, α-quartz present in the raw material undergoes a displacive transition into β-quartz, a reversible rearrangement without major structural breakdown. The small weight loss at 900 °C indicates minor volatilization without significant decomposition. The most critical transformations occur between 1250 °C and 1430 °C, marked by a weak weight loss at 1330 °C and a sharp endothermic peak at 1430 °C. In this high-temperature regime, two irreversible processes dominate: (i) β-quartz reconstructively transforms into cristobalite, and (ii) kyanite decomposes to produce mullite and free silica (either amorphous or crystalline). The full conversion of kyanite to mullite typically occurs between 1300 °C and 1435 °C, with the reaction accelerating as temperature approaches the upper limit [97,98].

From a processing perspective, these transformations are of central importance: Secar 80 provides a transient matrix that gradually converts into thermally stable phases, while kyanite acts as a reactive aluminosilicate source that strengthens the refractory network by in situ mullite crystallization. The synergy between these two raw materials underpins the design of castables with enhanced high-temperature mechanical strength, reduced thermal expansion, and improved slag resistance.

3.3.2. High-Temperature XRD (Thermodiffraction) Analysis of Secar 80 and Kyanite

The crystallographic evolution of Secar 80 (hydraulic calcium aluminate cement) and kyanite (Al_2SiO_5, a mullite precursor) was monitored by in situ high-temperature X-ray diffraction (HT-XRD) using an Anton Paar HTK 16N chamber, with operational capability up to 1600 °C. The analysis was carried out at selected transformation points previously identified through TGA–SDTA, namely 25, 150, 580, 900, 1250, 1330, 1430, and 1500 °C. This combined approach allowed the identification of metastable intermediates and stable high-temperature phases relevant to refractory performance.

High-Temperature XRD Analysis of Secar 80

The temperatures identified in the TGA–SDTA experiments guided the in situ HT-XRD analysis of Secar 80, with diffraction patterns collected in the 2θ range of 15–35° (Figure 6). These patterns reveal the progressive crystallographic transformations associated with the dehydration and decomposition of calcium aluminate cement (CAC) hydration products, capturing the sequence of hydration, dehydration, and eventual formation

of high-temperature anhydrous phases. At ambient temperature (25 °C) and 110 °C, the primary crystalline phases include gibbsite ($Al(OH)_3$), hydrated calcium aluminate (C_3AH_6), corundum (Al_2O_3), and monocalcium aluminate (CA). Gibbsite and C_3AH_6 arise from early hydration of CAC, whereas corundum and CA persist as unreacted or partially reacted clinker components. The presence of these phases aligns with previous thermal and diffraction studies, confirming their stability under low to moderately elevated temperatures [99–101]. Upon heating to 280 °C, gibbsite undergoes complete dehydration, as indicated by the disappearance of its characteristic reflections. This transformation, typically occurring between 240 and 317 °C, proceeds via intermediate boehmite (γ-AlOOH) formation, accompanied by water release [92,102]. Concurrently, the C_3AH_6 peaks decrease in intensity, reflecting the onset of structural water loss and progressive breakdown of hydrogarnet [103]. At this stage, mayenite ($C_{12}A_7$) emerges as a new crystalline phase, with its strongest reflection appearing at $2\theta \approx 18.03°$. Its formation is consistent with nucleation from precursor hydrates and minor kaolinite residues, generally becoming significant around 310 °C [104]. By 520 °C, C_3AH_6 has fully decomposed, leaving corundum, CA, mayenite, and minor platinum reflections from the sample holder as the dominant phases. This stage marks the transition from hydrated to anhydrous aluminates, an essential step for developing refractory properties. Between 680 °C and 960 °C, no major phase changes are observed; the system stabilizes with corundum, CA, and mayenite as the main constituents. Such stability reflects the refractory nature of these anhydrous phases following the early decomposition of hydrates [105,106]. Above 960 °C, calcium dialuminate (CA_2) begins to form as mayenite decomposes, with a concomitant increase in the intensity of both CA and CA_2 reflections up to 1270 °C. At 1350 °C, mayenite fully disappears, leaving corundum, CA, and CA_2 as the dominant phases. These three phases represent the most thermally stable assemblage in CAC systems and are critical for high-temperature performance [107].

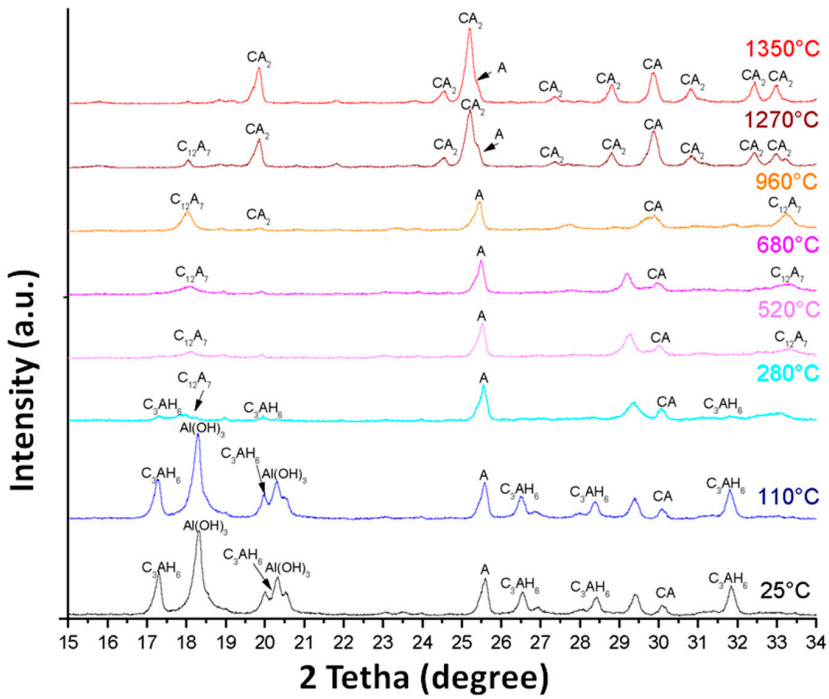

Figure 6. High-temperature XRD patterns of Secar 80, showing the evolution of crystalline phases: Gibbsite = ($Al(OH)_3$), Calcium aluminate hydrates = (C_3AH_6), Monocalcium aluminate = (CA), Monocalcium dialuminate = (CA_2), Mayenite = ($C_{12}A_7$), and A = Corundum (Al_2O_3).

In summary, the observed sequence demonstrates a progressive dehydration–decomposition pathway, where hydrated calcium aluminates sequentially lose water and

transform into anhydrous phases. The persistence of corundum, CA, and CA_2 at elevated temperatures underpins their mechanical strength, chemical durability, and resistance to thermal degradation, all of which are vital for refractory applications [108,109]. Moreover, the completeness of these transformations is influenced by the CaO/Al_2O_3 ratio, sintering temperature, and dwell time, with higher temperatures and optimal compositions promoting the formation of a stable anhydrous microstructure [110,111].

High-Temperature XRD Analysis of Kyanite

High-temperature X-ray diffraction (HT-XRD) experiments were conducted on kyanite using the temperature points determined from TGA–SDTA. Figure 7 presents the diffraction patterns collected in the 2θ range of 20–40°, chosen to highlight the evolution of the principal crystalline phases.

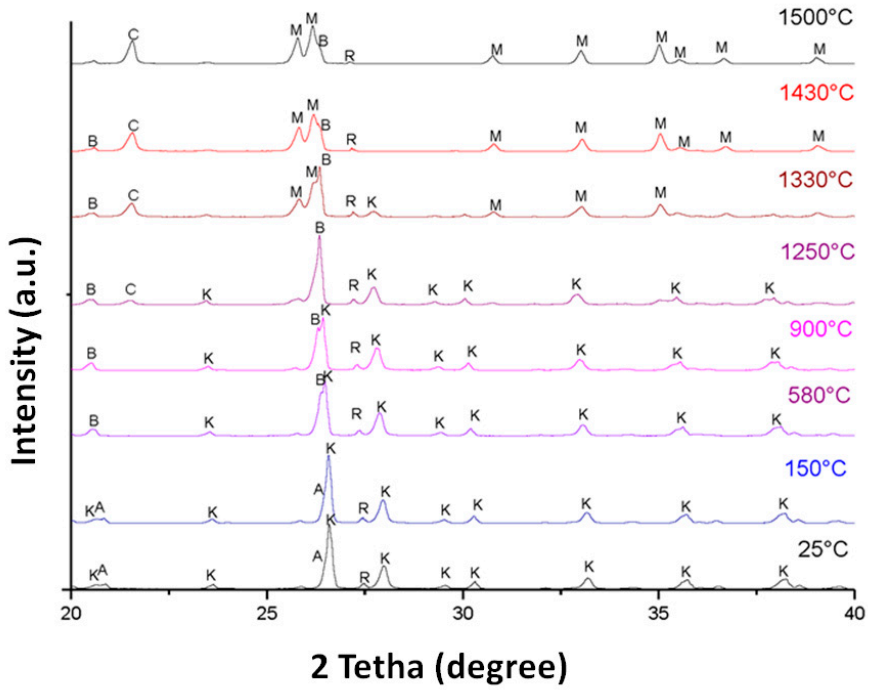

Figure 7. High-temperature XRD comparison for K = Kyanite (Al_2SiO_5), A = α-quartz (α-SiO_2), B = β-quartz (β-SiO_2), C = Cristobalite (SiO_2), R = Rutile (TiO_2), M = Mullite ($Al_{4.52}Si_{1.48}O_{9.74}$).

At room temperature, the primary phases identified were kyanite (Al_2SiO_5), α-quartz (SiO_2), and rutile (TiO_2). No structural changes were observed up to 150 °C, consistent with the known thermal stability of these phases at low to moderate temperatures. At 580 °C, kyanite remains metastable, exhibiting slight changes in lattice parameters without a complete structural transformation. This behavior aligns with previous studies on Al_2SiO_5 polymorphs, which indicate that kyanite can persist outside its equilibrium field under progressive heating due to kinetic barriers and accommodates thermal expansion through subtle lattice distortions rather than full reconstructive transformations [77,112,113]. By 900 °C, α-quartz undergoes a displacive phase transition to β-quartz, characterized by a continuous lattice rearrangement primarily involving tilting of SiO_4 tetrahedra. This transformation is typically reversible upon cooling and does not involve significant diffusion of atoms [114–116]. Throughout this temperature interval, both kyanite and rutile remain structurally stable, reflecting their inherent refractory behavior [117].

Significant mineralogical changes occur between 1250 and 1330 °C. Kyanite decomposes, and mullite ($Al_{4.52}Si_{1.48}O_{9.74}$) begins to form, following the well-established reaction:

$$3\ Al_2O_3{\cdot}SiO_2 \rightarrow 3Al_2O_3{\cdot}2SiO_2\ (\text{mullite}) + SiO_2 \quad (9)$$

The liberated silica often crystallizes as β-cristobalite at these high temperatures. The transformation of kyanite to mullite generally initiates around 1320 °C and completes by 1400 °C, often involving transient liquid phases that facilitate nucleation and growth. Mullite morphology evolves from fine needle-like structures at the onset of formation to platelet-like grains at higher temperatures, enhancing mechanical strength and thermal stability [74,76]. Simultaneously, β-cristobalite emerges from β-quartz through a reconstructive transformation, facilitated by elevated temperatures and the presence of silica released from kyanite decomposition. The kinetics of mullite formation are influenced by the availability of free silica, with quartz acting as both a reactant and nucleation site [118–120]. At 1430–1500 °C, the crystalline assemblage is dominated by mullite and β-cristobalite, with minor residual β-quartz and rutile. This phase composition is typical for high-temperature treatment of aluminosilicate ceramics, such as kaolinitic clays and refractory fibers. The persistence of some β-quartz is attributed to kinetic limitations, incomplete transformation, or local compositional variations [119]. Rutile remains stable as a minor phase throughout the temperature range, consistent with its refractory nature [121]. The dominance of mullite and β-cristobalite at elevated temperatures is critical for refractory and ceramic applications, as these phases confer high mechanical strength, low thermal conductivity, and excellent thermal shock resistance [69].

The HT-XRD results complement the TGA–SDTA data, confirming the critical temperature ranges for kyanite decomposition, quartz polymorphic transitions, and the formation of thermally stable phases.

3.4. Microstructure

3.4.1. Control Specimen (CC)

The microstructural characteristics of the control specimen sintered at 1400 °C are shown in Figure 8. The backscattered electron (BSE) image reveals a heterogeneous microstructure consisting of coarse to medium-sized aggregates (~1 mm to 50 µm) uniformly distributed within the refractory body. These aggregates display predominantly subangular morphologies and are partially embedded in a finer-grained matrix (<50 µm), consistent with the microstructural features reported for aluminosilicate based castables [1,2]. EDS analysis identified the aggregates as mainly corundum, which forms the rigid skeleton of the microstructure and provides resistance to thermal and mechanical stresses. The surrounding matrix is primarily composed of mullite, with minor quantities of anorthite, both of which are phases typically associated with high refractoriness and mechanical integrity at elevated temperatures. However, the microstructure also exhibits several limiting features. Significant residual porosity is observed both within the aggregates and in the matrix, accompanied by transgranular and interfacial microcracks. These defects highlight the incomplete densification achieved at 1400 °C. The persistence of porosity is attributed to the release of chemically bound water from calcium aluminate hydrates above 200 °C, which generates microvoids that are not completely eliminated during firing. In addition, insufficient liquid-phase formation and ceramic bonding restrict the consolidation of the structure, leading to discontinuities that undermine load transfer across the microstructure.

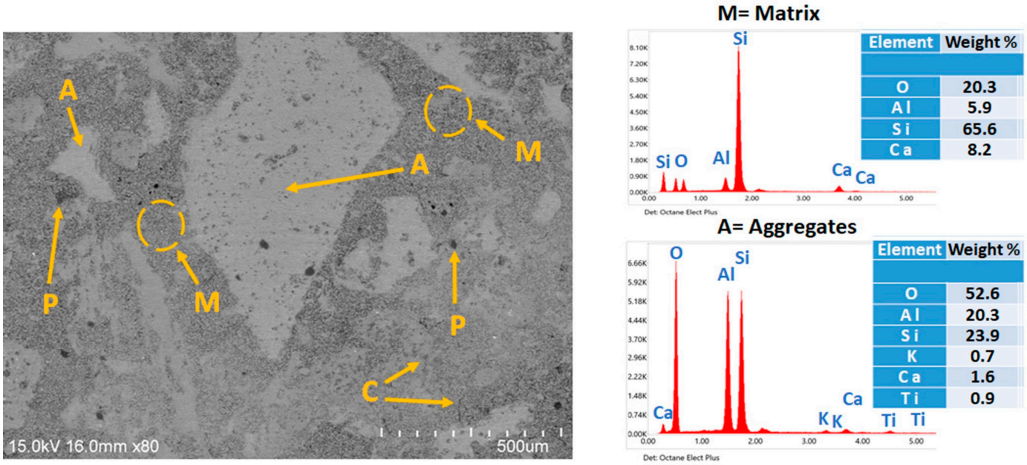

Figure 8. Micrograph and EDS analysis of the CC refractory specimen obtained at 1400 °C, where M = Matrix, A = Aggregates, C = Microcracks, and P = Porosity.

The microstructural evidence suggests that, although the control formulation develops a stable skeleton of corundum and a supporting mullite–anorthite matrix, its sintering efficiency at 1400 °C remains limited. The combination of residual porosity and weak aggregate–matrix interfaces in the CC composition could be detrimental for mechano-physical performance compared to the chamotte-modified compositions [23].

3.4.2. 5CH

The microstructural features of the 5CH specimen sintered at 1400 °C are presented in Figure 9. The backscattered electron (BSE) micrograph shows a well-consolidated microstructure with aggregates uniformly distributed across a wide particle size range and effectively bonded by a continuous matrix. EDS elemental analysis confirmed that the aggregates are primarily corundum, whereas the matrix consists of mullite and anorthite, in good agreement with the crystalline phases detected by XRD (Figure 2).

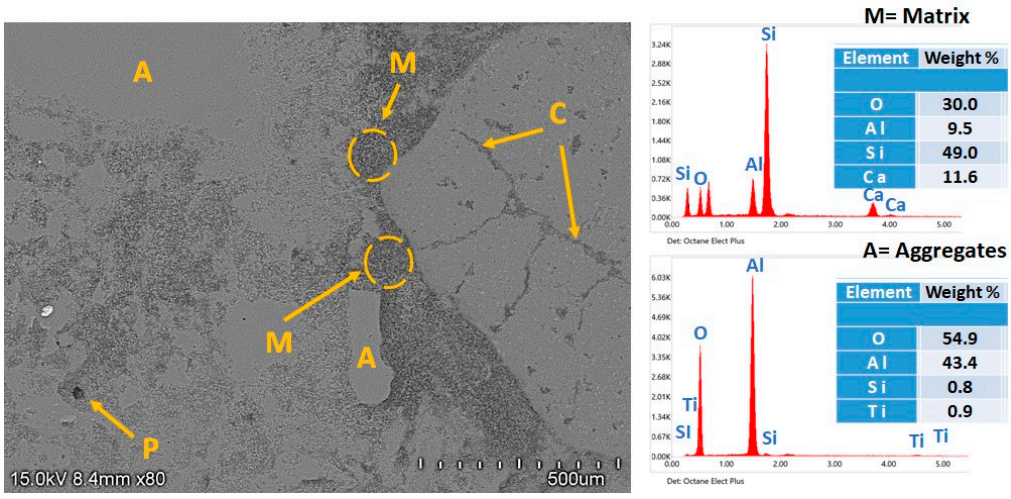

Figure 9. Micrograph and EDS analysis of the 5CH refractory specimen obtained at 1400 °C, where M = Matrix, A = Aggregates, C = Microcracks, and P = Porosity.

The addition of chamotte significantly modified the microstructural development compared to the control specimen. A key difference is the enhanced aggregate densification, which is attributed to the in situ formation of secondary mullite needles within the matrix. These elongated crystals, exhibiting an interlocked morphology, bridge adjacent particles and promote a stronger ceramic bond. Their reinforcing action improves the packing

density, reduces microstructural discontinuities, and is expected to translate into superior mechanical strength and thermal stability [122].

Chamotte also played a decisive role in tailoring the porosity characteristics. In addition to the pores within aggregates and the matrix-related microcracks observed in the control composition, the 5CH specimen exhibited rounded, isolated (closed-type) pores distributed within the matrix. This type of spherical porosity, typically associated with limited liquid-phase formation during high-temperature firing, can be beneficial. Closed pores reduce stress concentration sites and act as crack deflectors, thereby retarding microcrack propagation and enhancing thermal shock resistance. Moreover, the coexistence of secondary mullite reinforcement and closed porosity indicates a more optimized microstructure in which strength and toughness are balanced, improving the refractory's long-term serviceability [23].

3.4.3. 10CH

The microstructural characteristics of the 10CH refractory specimen sintered at 1400 °C are presented in Figure 10. EDS elemental mapping confirmed corundum as the dominant aggregate phase, providing a mechanically robust backbone, while mullite and anorthite were identified in the matrix. The BSE micrograph revealed a well-sintered and highly consolidated structure, with aggregates uniformly distributed across a broad particle size range and firmly bonded by a continuous ceramic matrix. Compared to lower chamotte additions, the 10CH specimen exhibited superior densification, reflecting improved sinterability. This enhancement is attributed to the combined effect of chamotte particles, which act as stable refractory skeletons, and the in situ generation of secondary mullite and anorthite, which strengthen the interparticle bonds and promote microstructural continuity [122–124].

Secondary mullite, in particular, formed as elongated, needle-like crystals bridging adjacent grains. These structural linkages closed microstructural voids and refined the pore structure, leading to a reduction in both pore size and connectivity. Moreover, their interlocked morphology effectively restricted microcrack propagation, improving fracture resistance and thermal shock stability [125,126]. The presence of rounded closed pores—smaller and fewer than in 5CH—further suggests partial liquid-phase sintering, which contributed to stress redistribution and additional crack deflection mechanisms.

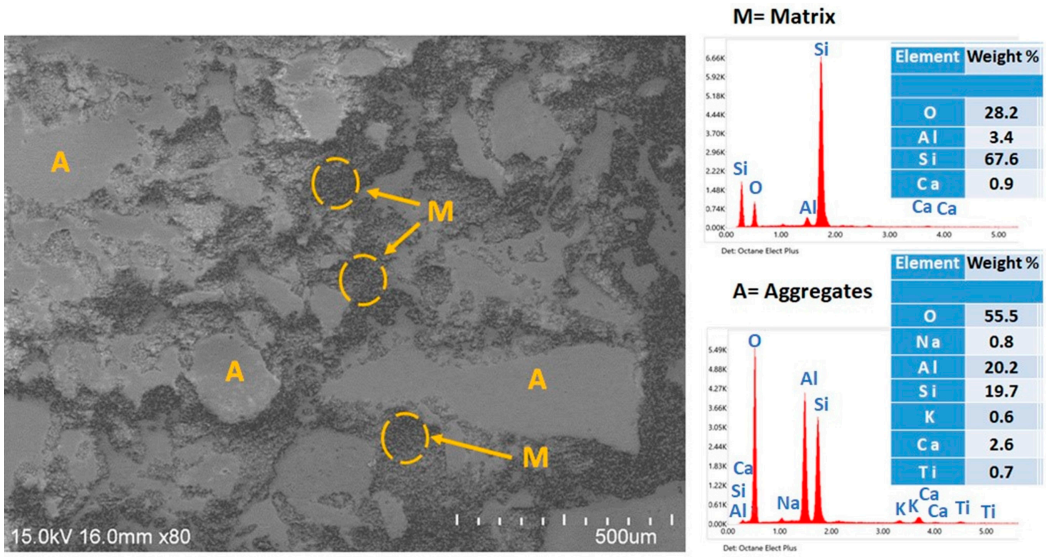

Figure 10. Micrograph and EDS analysis of the 10CH refractory specimen obtained at 1400 °C, where M = Matrix, A = Aggregates.

3.5. Physical Properties of Refractory Specimens

The physical properties of the experimental refractory specimens—specifically apparent porosity (Figure 11) and bulk density (Figure 12)—were evaluated at 110, 815, 1050, and 1400 °C to investigate the effects of firing temperature and the incorporation of chamotte waste from rejected fired electrical porcelain on the refractory matrix.

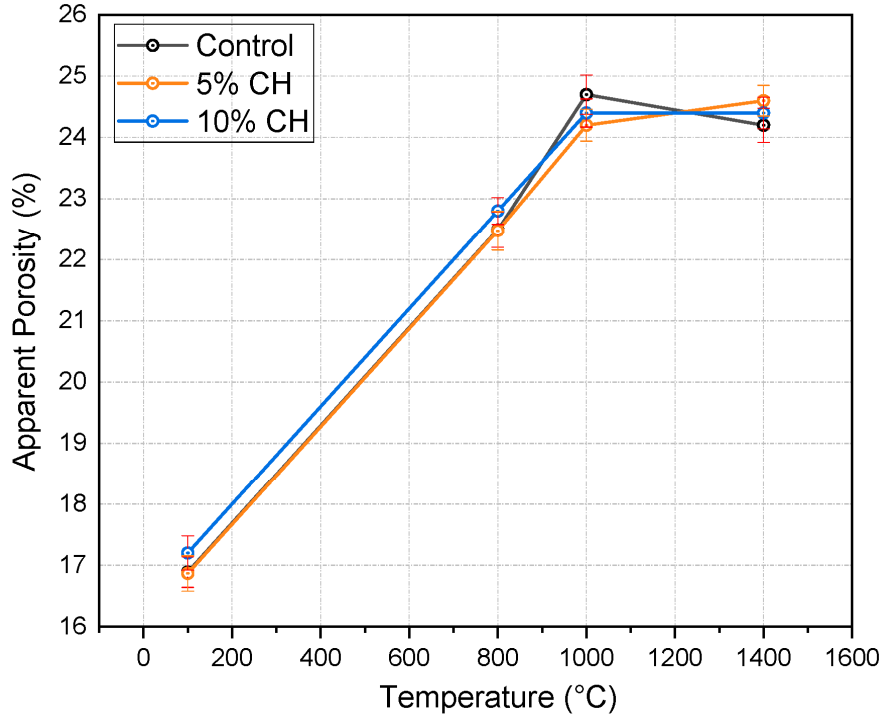

Figure 11. Apparent porosity of Control, 5CH, and 10CH compositions as a function of firing temperature.

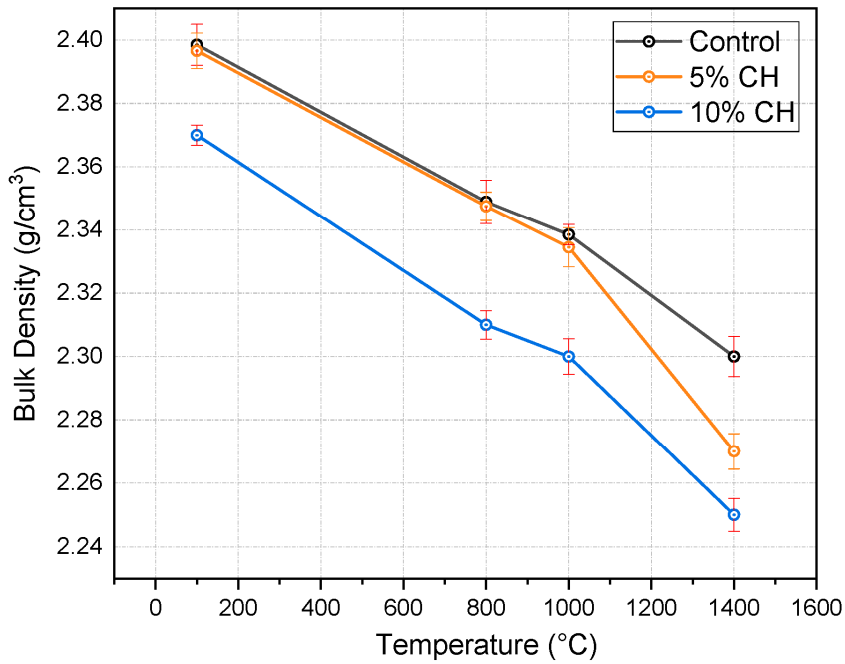

Figure 12. Bulk density of Control, 5CH, and 10CH compositions as a function of firing temperature.

At 110 °C, the 5CH composition exhibited the lowest apparent porosity (16.8%) while maintaining the same bulk density (2.4 g/cm^3) as the control composition. The unchanged

bulk density can be explained by the partial substitution of flint clay (1.99–2.60 g/cm^3) with recycled chamotte, a by-product of comparable density (2.40–2.58 g/cm^3). The observed porosity reduction is attributed to the finer particle size of chamotte ($d_{50} \approx 26$ µm), which enhances particle packing, minimizes voids, and improves mass distribution within the castable matrix. This microstructural refinement not only promotes densification but also might contribute to improved mechanical reliability. Fine chamotte particles contribute to increased bulk density, while the influence of packing becomes less pronounced as the proportion of bonding clay rises [127]. Studies in geopolymer and refractory systems confirm that moderate additions of chamotte (up to ~20 wt.%) enhance mechanical strength and density, whereas excessive incorporation can reduce workability but improve shape retention [27,128]. In the 10CH specimen, porosity was slightly higher (17.2%), with bulk density unchanged, indicating that the beneficial effects of chamotte inclusion at low temperatures are maintained up to 10 wt.%.

In refractory castables, early particle bonding is governed by the hydraulic setting of calcium aluminate cement, which generates metastable hydrates such as CAH_{10}, C_2AH_8, and amorphous AH_3 upon mixing with water [129]. With increasing temperature, physically bound and capillary-retained water is progressively released, while these metastable hydrates convert into more stable phases, primarily C_3AH_6 and crystalline AH_3 (gibbsite). This dehydration–conversion sequence induces volumetric instability, which might manifest as a reduction in bulk density, most pronounced near 815 °C. In formulations containing 5–10 wt.% chamotte, the effect could be amplified by the higher quartz content. The α–β quartz polymorphic transformation at ~573 °C further contributes to volumetric fluctuations, generating microcracking and rearrangements that hinder densification and compromise mechanical reliability [130,131]. However, as shown Figure 12, bulk density remained essentially constant (≈2.3 g/cm^3), suggesting that the mass loss from dehydration did not significantly compromise the structural framework.

Meanwhile, when the firing temperature increased to 815 °C, porosity increased in all formulations, reaching 22.4% for the control and 5CH compositions and 22.8% for 10CH. This behavior is consistent with the more complex thermal transformations occurring in chamotte-containing compositions. In the range up to 815 °C, porosity evolution is mainly governed by two mechanisms: (i) dehydration of hydration products and (ii) the polymorphic transformation of quartz. Between 110 and 300 °C, free and bound water are released from AH_X gels, accompanied by the decomposition of metastable hydrates such as CAH_{10} and C_2AH_8. At ~370 °C, more stable phases (C_3AH_6 and crystalline AH_3) further decompose, generating additional porosity. In parallel, chamotte-rich specimens undergo the $\alpha \rightarrow \beta$ quartz transition near 573 °C, which induces localized volumetric expansion and microcracking. The extent of this transformation scales with quartz content, amplifying internal stresses and pore formation.

The combined effects of hydrate decomposition and quartz allotropic expansion explain the higher porosity observed in chamotte-modified castables compared to the control [24,132–135].

This combined behavior shows at 815 °C is typical in alumina-based ceramics and calcium aluminate systems, where initial dehydration increases porosity without drastically altering overall density [136,137].

At 1050 °C, all refractory specimens exhibited a further rise in apparent porosity, mainly due to the breakdown of the hydraulic bond. At this temperature, the porosity stabilized with values of 24.7%, 24.2%, and 24.4% for the control, 5CH, and 10CH compositions, respectively. This values results from the dissociation of hydration-derived phases, including CAH_{10}, C_2AH_8, and particularly C_3AH_6, whose dehydration yields $C_{12}A_7$, free CaO, and water vapor.

Concurrently, the decomposition of crystalline AH_3 produces boehmite (AlO(OH)), which subsequently transforms into amorphous Al_2O_3 and H_2O. These reactions, occurring between 815 and 1050 °C, weaken the matrix continuity and generate additional pores.

Despite this increase in poverty, beneficial microstructural rearrangements also emerge. Around 1000 °C, in situ secondary mullite begins to crystallize, forming interlocking needle-like morphologies that gradually strengthen the ceramic bond. This mullite development partially offsets the negative effects of porosity, laying the foundation for enhanced thermal stability and long-term mechanical reliability of the refractory castables [130,138–141].

As the firing temperature rises to 1050 °C, a progressive decrease in bulk density is observed across all refractory specimens, with the 10CH formulation exhibiting the most significant reduction. By contrast, the control and 5CH specimens show only a moderate decline, which can be linked to enhanced crystallization and localized sintering phenomena at intermediate temperatures.

The additional amorphous silica contributed by chamotte favors the generation of a SiO_2-rich transient liquid phase, which improves atomic diffusion pathways and facilitates the dissolution of fine Al_2O_3 particles. This reactive environment promotes the in situ precipitation of secondary mullite, whose elongated, interlocking needles progressively fill and bridge pores. Such microstructural reinforcement partially offsets the densification loss by reducing open porosity and improving particle packing efficiency, thereby yielding a more stable bulk density profile in the control and 5CH compositions [125,141–143].

In summary, bulk density remained nearly constant (≈2.3 g/cm^3), consistent with previous reports showing that volumetric changes associated with the decomposition of calcium aluminate hydrates (e.g., formation of C_3AH_6) modify pore morphology without significantly affecting bulk density [110,144]. Pore size distributions may shift toward larger or secondary pores while total porosity remains similar. This balance between mass loss and densification from newly formed crystalline phases explains the observed stability in bulk density [145].

At 1400 °C, partial densification occurred in all formulations, with the 10CH and 5CH compositions showing comparable porosity, 24.4% and 24.6%, respectively, compared to 24.2% for the control composition. This behavior can be attributed to the onset of liquid-phase sintering, where low-viscosity aluminosilicate melts partially fill pores and enhance particle rearrangement. The extent of densification depends on the aluminosilicate content of chamotte and the formation of high-temperature phases such as mullite [146,147]. In the present study, the thermal cycle was sufficient to promote minor densification but did not significantly alter bulk density, which remained at 2.3 g/cm^3. Inadequate liquid-phase formation or suboptimal sintering conditions may limit densification, whereas excessive liquid or gas entrapment can paradoxically increase porosity [148–150].

These findings demonstrate that incorporating up to 10 wt.% chamotte waste enhances packing efficiency due to its fine particle size ($d_{50} \approx 26$ µm), which reduces voids and promotes a more homogeneous mass distribution within the castable matrix. Despite this modification, bulk density remains essentially unchanged, reflecting the comparable density of chamotte to flint clay. At firing temperatures above 1000 °C, the dominant effects are associated with phase evolution and microstructural rearrangements—such as secondary mullite and anorthite formation—rather than extensive densification, highlighting the functional role of chamotte as both a recycled raw material and a microstructural stabilizer. These insights are relevant for designing sustainable refractory compositions with controlled porosity and thermal stability.

3.6. Mechanical Behavior of Refractory Samples

3.6.1. Cold Crushing Strength (CCS)

The mechanical performance of the developed refractories was assessed through cold crushing strength (CCS) and modulus of rupture (MOR) tests, aiming to establish correlations between mechanical behavior, composition design, and firing temperature. Specimens corresponding to the three compositions (Control, 5CH, and 10CH) were evaluated after curing (110 °C) and at elevated temperatures of 815, 1050, and 1400 °C. These results provide insight into the balance between hydraulic bonding at low temperatures and ceramic bonding at higher firing stages.

Figure 13 presents the CCS evolution of the three formulations. At 110 °C, the 10CH specimen developed the greatest compressive strength (39.4 MPa), exceeding the values obtained for the 5CH (38.6 MPa) and the Control (34.7 MPa) specimens. The observed enhancement in strength at ambient curing conditions can be attributed to the development of hydraulic bonds and the precipitation of cohesive hydration products, primarily CAH_{10} and C_3AH_6. These phases originate from the reaction of calcium aluminate cement with mixing water, effectively binding the solid particles and imparting early mechanical integrity to the refractory matrix [151,152]. In addition, the finer particle size of chamotte contributes to more efficient particle packing within the castable, reducing intergranular voids and enhancing mass distribution throughout the matrix. This microstructural refinement promotes better packing density and supports the development of a more homogeneous load-bearing network. Consequently, the castable exhibits not only improved densification but also enhanced mechanical reliability, as the refined packing limits stress concentrations, restricts crack initiation, and increases the overall structural integrity under thermal and mechanical loads.

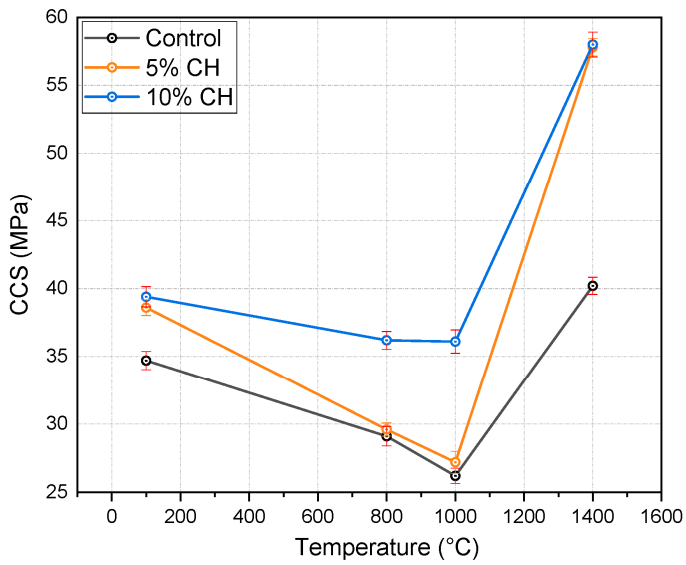

Figure 13. Cold Crushing Strength (CCS) vs. firing temperature for Control, 5CH, and 10CH compositions.

Evaluating mechanical strength at 110 °C is essential since it reflects the castable's performance during drying and early service conditions. At this stage, free water is removed while hydraulic bonds from aluminous cement hydration (CAH_{10}, C_2AH_8, C_3AH_6) provide mechanical integrity. Sufficient strength ensures safe handling, prevents spalling during preheating, and indicates reliable transition to high-temperature operation before ceramic bonding develops.

As is known, at 110 °C, the castables are only dried, not sintered. In this condition, water physically bound within pores and capillaries is removed without inducing signif-

icant phase transformations, volume changes, or stresses. The microstructure remains relatively intact, with no microcracking or porosity increase. As a result, mechanical tests reflect the inherent particle packing and the hydraulic bonding provided by calcium aluminate cement, which is strongest in this dried state. Therefore, the superior mechanical properties at 110 °C arise from the intact hydraulic bonding network and absence of microstructural damage.

Between 110 and 815 °C, all compositions experienced a pronounced reduction in CCS, with values of 36.2 MPa for 10CH, 29.6 MPa for 5CH, and 29.1 MPa for the Control specimen. This decrease is associated with the dehydration of calcium aluminate hydrates (e.g., CAH_{10}, C_2AH_8, C_3AH_6), which destabilizes the cementitious network and increases porosity through water release. The degradation of hydraulic bonds without the simultaneous development of ceramic bonds produces a temporary mechanical weakness, a well-reported transitional stage in alumina–cement refractories. Furthermore, the onset of phase rearrangements—particularly the conversion of aluminous hydrates into more stable crystalline phases—introduces microcracking and structural discontinuities, further amplifying strength losses [143,153].

At 1050 °C, the Control (26.2 MPa) and 5CH (27.2 MPa) specimen displayed a further decline in compressive strength, indicating that the establishment of ceramic bonding remained incipient. At this stage, the thermal energy is insufficient to promote extensive particle rearrangement and solid-state diffusion, resulting in weak grain–grain contacts, inadequate neck growth, and limited densification [130,133,151]. In contrast, the 10CH specimen exhibited a marked strength increase (36.1 MPa). This recovery in CCS is associated with phase evolution processes that favor the onset of a ceramic bond, particularly the in situ crystallization of secondary mullite from the reaction of alumina with a silica-rich transient liquid phase. The interlocking, acicular morphology of these mullite crystals provides a reinforcing effect by bridging pores (reduces pore connectivity), restricting crack propagation, and enhancing load transfer across the matrix. Also, the literature on aluminosilicate-based refractories highlights that the initiation of sintering in this temperature range reduces pore connectivity and contributes to strength recovery [143,154].

Nevertheless, the role of residual free silica must be considered, as its polymorphic transition from α- to β-quartz (~573 °C) can generate volumetric fluctuations and microcracking. The superior performance of the 10CH castable suggests that the greater amount of secondary mullite formed in this formulation offset the destabilizing effects of silica expansion, leading to a more coherent and stable microstructure. Such behavior highlights the capacity of recycled chamotte not only to serve as a sustainable raw material but also to promote microstructural reinforcement at intermediate firing temperatures. This performance is particularly relevant for industries such as aluminum, cement, and petrochemical processing, where refractory components are often used below steelmaking temperatures. Achieving enhanced strength in this range could reduce sintering energy requirements during manufacturing, while simultaneously improving service reliability [139,155].

Summarizing the mechanical behavior at low and intermediate temperatures, between 110 and 815 °C, several deleterious processes occur before effective sintering densification can dominate, affecting mechanical properties: (i) Dehydration and decarbonation reactions; calcium aluminate hydrates (CAH_{10}, C_2AH_8, C_3AH_6) and other hydrated phases decompose, releasing structural water. This creates new porosity, weakening the microstructure before sufficient high-temperature bonding develops. (ii) Phase transformations with volume instability: quartz undergoes the α–β transition near 573 °C, generating thermal stresses and microcracks. In addition, partial mullitization may initiate, but incomplete growth results in weak, porous bonding rather than strengthening. (iii) Insufficient sintering at intermediate temperatures: at 815–1050 °C, sintering is not yet strong enough to

counteract porosity increase and microcrack formation. Thus, strength decreases compared to the dried state.

Intermediate temperatures (815–1050 °C) induce hydration decomposition, quartz transitions, and microcracking without sufficient sintering to compensate.

At 1400 °C, the strengthening effect became more evident. The 10CH formulation reached the highest CCS (58 MPa), approximately 44% above the Control sample (40.2 MPa), demonstrating the beneficial role of chamotte porcelain waste. This improvement is attributed to the combined crystallization of mullite and anorthite, which generate strong ceramic bonds and promote effective pore filling. Mullite contributes to mechanical and thermal stability due to its high Young's modulus (~170–180 GPa) and low thermal expansion (~5×10^{-6} K^{-1}), while anorthite enhances densification by providing a low-viscosity liquid phase that seals residual pores.

The synergy between these phases results in a denser, interlocked microstructure capable of sustaining higher compressive loads. Microstructurally, the combined effects of (i) homogeneous phase distribution, (ii) enhanced sintering of the aggregate phase, and (iii) controlled refinement of the pore structure endowed the 10CH composition with the highest mechanical strength among all tested refractories. These results highlight that an optimal chamotte waste ratio not only reduces porosity but also promotes a reinforcing microstructural framework, making 10CH the most structurally resilient and sustainable composition within this study [139,155].

The final compressive strength results indicate that the incorporation of chamotte porcelain waste enhances high-temperature strength development, particularly at 1400 °C, where ceramic bonding dominates. The findings demonstrate that controlled chamotte waste additions not only maintain early mechanical integrity but also substantially improve long-term refractory performance, supporting their viability as a sustainable raw material in high-temperature applications.

In summary, at higher firing (≈1400 °C), sintering and mullite/anorthite formation dominate, healing pores, reducing cracks, and creating strong thermomechanical bonds—finally improving strength beyond the 110 °C baseline.

3.6.2. Modulus of Rupture (MOR)

Figure 14 presents the modulus of rupture (MOR) of the Control, 5CH, and 10CH composition as a function of firing temperature. At 110 °C, the 10CH specimen exhibited the highest MOR (16.1 MPa), followed by 5CH (14.7 MPa) and then the Control specimen (14.2 MPa). This trend reflects the dominance of hydraulic bonding at low curing temperatures, where the formation of calcium aluminate hydrates (CAH_{10}, C_2AH_8, and C_3AH_6) provides a compact matrix and stronger flexural resistance.

The superior mechanical response observed at 110 °C is primarily attributed to the preservation of the hydraulic bonding network formed during curing. At this stage, hydration products such as CAH_{10}, C_2AH_8, and C_3AH_6 remain structurally intact, ensuring effective particle cohesion. Moreover, the absence of significant dehydration, phase conversion, or thermally induced stresses prevents microstructural damage, allowing the refractory matrix to retain its early strength and integrity.

At 815 °C, a marked reduction in the modulus of rupture (MOR) was observed across all formulations, with values of 8.4 MPa for 10CH, 8.2 MPa for 5CH, and 6.5 MPa for the Control specimen. This decline is attributed to the complete decomposition of calcium aluminate hydrates, resulting in the collapse of the hydraulic bond and the formation of a porous, weakened microstructure. The dehydration of phases such as CAH_{10} and C_3AH_6 in this range is well documented to generate structural instability, which disrupts load transfer pathways and lowers flexural capacity [156]. The mechanism mirrors

the degradation reported in other hydraulically bonded systems—such as fibercement boards and geopolymer composites—where thermal exposure leads to bond deterioration and increased crack susceptibility [157]. At this stage, the refractory relies solely on physical particle contacts, with limited sintering or phase development to recover mechanical strength.

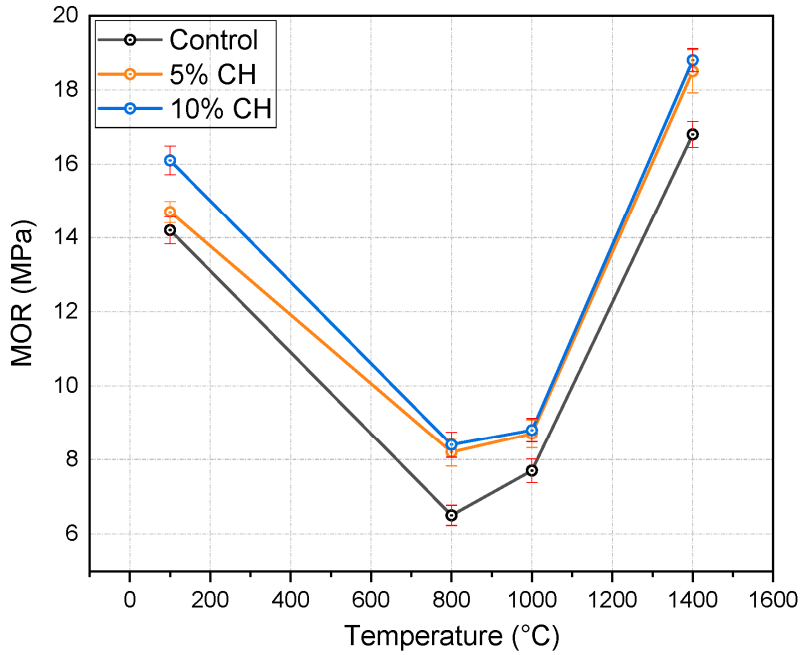

Figure 14. Modulus of Rupture (MOR) vs. firing temperature for Control, 5CH, and 10CH compositions.

At 1050 °C, both 10CH (8.8 MPa) and 5CH (8.7 MPa) exhibited a moderate recovery in MOR, while the Control composition remained comparatively lower (7.7 MPa). This increase signals the onset of ceramic bonding through initial sintering and crystallization of thermodynamically stable phases. Literature confirms that the progressive formation of mullite, spinels, or β-SiAlON at intermediate firing temperatures contributes to densification, stronger interfacial contacts, and crack-bridging effects, which enhance flexural resistance [158,159]. In particular, mullite's needle-like morphology provides efficient stress transfer across grain boundaries, while other ceramic phases contribute to pore refinement and structural integrity [160]. The observed recovery of MOR in chamotte-containing samples highlights the role of chamotte waste as a reactive source that promotes the nucleation of these ceramic phases earlier than in the Control composition.

At 1400 °C, the 10CH composition achieved the highest MOR (18.8 MPa), approximately 32% greater than the Control composition (16.8 MPa). This improvement results from advanced sintering and extensive phase evolution, primarily the crystallization of mullite and anorthite. Both phases contribute synergistically: mullite offers high thermal stability and mechanical stiffness, while anorthite enhances densification by filling residual pores and reinforcing grain boundaries [161,162]. The formation of interlocked, needle-shaped mullite crystals further improves flexural resistance by inhibiting crack propagation and enhancing grain interlocking, which is particularly beneficial under thermal shock conditions common in service environments [81]. Efficient densification at this stage significantly reduces porosity and strengthens ceramic bonding, leading to the superior performance of 10CH composition.

A clear structure–property relationship emerges when comparing the MOR and CCS results with the microstructural and phase analysis. The 10CH composition, characterized by higher mullite and anorthite contents and reduced porosity at 1400 °C (as confirmed

by XRD and microstructural observations), achieved simultaneous improvements of ~44% in CCS and ~32% in MOR relative to the Control composition. This dual improvement highlights that chamotte addition, when optimized, not only reduces raw material cost by valorizing industrial waste but also strengthens long-term refractory performance by enabling phase assemblages that are thermomechanically stable. Mullite provided a stiff, interlocked skeleton that improved both compressive and bending resistance, while anorthite acted as a densifying phase, sealing pores and strengthening grain boundaries. In contrast, the Control and 5CH compositions, with lower mullite content and higher residual porosity, exhibited inferior flexural and compressive strength. These findings underscore the importance of optimized chamotte incorporation in calcium aluminate cement (CAC)-bonded refractories as a strategy to achieve superior mechanical reliability under high-temperature service conditions.

3.7. Environmental and Sustainability Implications of Chamotte-Modified Refractory Castables

Advancing refractory technologies requires balancing high-performance demands with urgent sustainability targets. The incorporation of industrial by-products into refractory formulations addresses both needs by conserving finite mineral resources and reducing the environmental burdens associated with virgin raw material extraction and energy-intensive processing [153,154,163,164]. In this context, chamotte emerges as a particularly valuable resource. Despite its global abundance, current reuse and recycling rates remain low. Valorizing this underutilized by-product as a functional raw material not only supports circular economy objectives but also contributes to reducing waste streams and minimizing the environmental footprint of refractory production [23,39,165,166].

The environmental advantages of chamotte incorporation extend beyond waste diversion. Substituting virgin aluminosilicate feedstocks with chamotte significantly lowers cumulative energy demand and greenhouse gas (GHG) emissions by reducing reliance on high-temperature processing and large-scale mining operations. Such reductions in embodied carbon are particularly relevant for refractories used in energy-intensive industries, where decarbonization pathways are increasingly prioritized.

From a technical standpoint, the 10CH composition (10 wt.% chamotte) demonstrated superior physical and mechanical performance relative to the control composition. These improvements stem from favorable microstructural evolution, including the in situ formation of interlocked mullite needles and anorthite phases, which promote densification, reduce porosity, and reinforce grain boundaries [122,133].

This phase assemblage enhances both mechanical strength and thermal stability, providing resilience against thermal cycling and mechanical loading—key requirements for industrial service.

Economically, chamotte functions as both a performance-enhancing component and a cost-effective filler, decreasing reliance on expensive, high-purity feedstocks. This dual role offers attractive cost–performance trade-offs, making chamotte-modified castables highly suitable for biomass-fired boilers, where durability under alkali-rich conditions, cyclic thermal shocks, and material affordability are critical.

Despite these promising outcomes, further studies are needed to confirm long-term applicability. Future research should focus on thermal shock resistance, alkali slag corrosion, and cyclic fatigue testing under industrially relevant conditions. Additionally, cradle-to-gate life cycle assessments (LCA) are essential to quantify reductions in energy consumption, GHG emissions, and resource depletion compared to conventional castables. Coupled with techno-economic analyses, such studies will provide robust evidence of the environmental and economic advantages of chamotte-based refractories.

Chamotte incorporation represents a practical and scalable strategy to reduce the environmental footprint of refractory castables while maintaining or enhancing technical performance. This approach aligns with cleaner production strategies and decarbonization targets in high-temperature industries, highlighting the potential of waste-derived raw materials to drive sustainable innovation in refractory manufacturing.

3.8. Limitations of Chamotte Recycling in Aluminosilicate Refractory Castables

Despite the promising results obtained in this study, several limitations must be acknowledged regarding the large-scale adoption of recycled chamotte in refractory castables. First, chamotte derived from diverse ceramic or refractory waste streams can exhibit significant variability in chemical composition, impurity content (e.g., Fe_2O_3, alkalis, and glaze phases), and particle morphology. This heterogeneity may compromise reproducibility and complicate industrial standardization. Moreover, residual metallic inclusions or glassy phases, even after magnetic cleaning, can alter phase equilibria at high temperatures and potentially reduce corrosion resistance under service conditions.

A second limitation relates to microstructural stability. While the formation of mullite and anorthite enhances densification and strength, heterogeneous distribution or excessive glassy phases may generate localized weak zones, limiting thermal shock resistance. Furthermore, the thermal stability of chamotte-based castables is constrained by the melting point of anorthite (~1553 °C), which restricts their use to moderate-temperature applications, such as biomass boilers, rather than high-temperature metallurgical processes.

Finally, industrial scalability requires careful evaluation. Crushing, milling, and cleaning operations are energy-intensive, and the overall techno-economic feasibility depends on balancing processing costs against raw material savings. Additionally, long-term durability under cyclic thermal loading, alkali vapor corrosion, and creep conditions remains insufficiently validated, necessitating extended service-life studies. Addressing these challenges will be critical to position chamotte as a reliable, standardized, and sustainable raw material in the refractory industry.

3.9. Future Work

Future research will focus on validating the long-term durability of chamotte-based refractory castables under service-relevant conditions. Particular emphasis will be placed on thermal shock resistance, due to the cyclic temperature fluctuations in biomass boilers, and on alkali vapor corrosion, a key degradation mechanism in biomass combustion. These studies are critical to confirm the suitability of the 10CH formulation for industrial applications.

In parallel, a cradle-to-gate life cycle assessment (LCA) will be conducted to quantify environmental benefits, including reductions in embodied energy, greenhouse gas emissions, and natural resource depletion. Techno-economic analyses will complement these efforts by assessing cost–performance trade-offs and benchmarking the proposed material against conventional refractory systems.

By combining durability testing with sustainability and economic assessments, future work will establish chamotte-modified castables as scalable, low-impact solutions that align with circular economy principles and contribute to the decarbonization of high-temperature industries.

4. Conclusions

The urgent need to promote circular economy strategies in the refractory industry underscores the importance of valorizing chamotte waste through sustainable manufacturing approaches. This study systematically evaluated the partial substitution of flint clay

fines with 5 and 10 wt.% chamotte in conventional aluminosilicate refractory castables, aiming to achieve an optimal balance between mechanical performance, thermal stability, and environmental sustainability.

Among all formulations, the 10CH composition demonstrated the most promising performance. After firing at 1400 °C, this formulation exhibited approximately 44% higher cold crushing strength (CCS) and 32% higher modulus of rupture (MOR) compared to the control specimen, while maintaining a bulk density of 2.25 g/cm^3 and an apparent porosity of 24.4%—values comparable to or slightly superior to conventional commercial aluminosilicate castables (typically 2.2–2.3 g/cm^3 and 24–26% porosity). These mechanical improvements were directly linked to the formation of thermomechanically stable crystalline phases, particularly secondary mullite and anorthite. The interlocked morphology of mullite enhanced the load-bearing capacity and fracture resistance, while anorthite contributed to densification by sealing intergranular voids and strengthening grain boundaries.

From a sustainability standpoint, the incorporation of 10 wt.% recycled chamotte significantly reduces the reliance on virgin flint clay resources, lowers material procurement costs, and contributes to waste minimization. The minimal compromise in densification confirms the technical feasibility of chamotte as a secondary raw material without sacrificing functional reliability or service performance.

Compared to conventional commercial aluminosilicate refractory castables, the developed formulations offer comparable or superior mechanical and microstructural performance, alongside notable environmental and economic advantages—including lower embodied energy, reduced CO_2 footprint, and enhanced resource efficiency. These outcomes position chamotte-based formulations as high-value sustainable alternatives for industrial applications in aluminum, cement, and petrochemical sectors operating at intermediate-to-high temperatures.

In summary, this research demonstrates that chamotte can be successfully valorized as a functional component in refractory castables, delivering technical benefits while advancing cleaner production goals. Future work should focus on life cycle assessment (LCA) and techno-economic analysis to quantify environmental savings and assess scalability for industrial adoption. Chamotte, once regarded as waste, thus emerges as a strategic raw material for low-carbon, high-performance refractory manufacturing.

Author Contributions: Conceptualization, L.D.-T. and E.A.R.-C.; methodology, L.D.-T., J.F.L.-P., Y.G.-C. and E.A.R.-C.; validation, E.A.R.-C. and J.E.C.d.L.; formal analysis, L.D.-T., J.F.L.-P., Y.G.-C. and E.A.R.-C.; investigation, L.D.-T. and E.A.R.-C.; resources, E.A.R.-C. and J.E.C.d.L.; writing—original draft preparation, L.D.-T., E.A.R.-C. and J.F.L.-P.; writing—review and editing, Y.G.-C., J.E.C.d.L. and E.A.R.-C.; visualization, L.D.-T. and E.A.R.-C.; supervision, E.A.R.-C.; project administration, E.A.R.-C. All authors have read and agreed to the published version of the manuscript.

Funding: This research received no external funding.

Institutional Review Board Statement: Not applicable.

Informed Consent Statement: Not applicable.

Data Availability Statement: The original contributions presented in this study are included in the article. Further inquiries can be directed to the corresponding author.

Acknowledgments: The first author gratefully acknowledges the Universidad Autónoma de Nuevo León (UANL) for providing access to analytical equipment, as well as the academic group of the Faculty of Mechanical Engineering (FIME) at UANL for their support. Special thanks are extended to M.Sc. Alberto Eliseo Montes Mejia for his valuable revisions and experimental guidance.

Conflicts of Interest: The authors declare no conflicts of interest.

References

1. Abou-Sekkina, M.M.; Abo-El-Enein, S.A.; Khalil, N.M.; Shalma, O.A. Phase Composition of Bauxite-Based Refractory Castables. *Ceram. Int.* **2011**, *37*, 411–418. [CrossRef]
2. Soltan, A.M.; Pöllmann, H.; Kaden, R.; König, A.; Abd El-Raoof, F.; Eltaher, M.; Serry, M. Degradation of Aluminosilicate Refractories: An Integrated Approach. *J. Eur. Ceram. Soc.* **2015**, *35*, 4573–4592. [CrossRef]
3. Aksel, C. The effect of mullite on the mechanical properties and thermal shock behaviour of alumina–mullite refractory materials. *Ceram. Int.* **2003**, *29*, 183–188. [CrossRef]
4. Spyridakos, A.; Alexakis, D.E.; Vryzidis, I.; Tsotsolas, N.; Varelidis, G.; Kagiaras, E. Waste Classification of Spent Refractory Materials to Achieve Sustainable Development Goals Exploiting Multiple Criteria Decision Aiding Approach. *Appl. Sci.* **2022**, *12*, 3016. [CrossRef]
5. Bezerra, B.; Luz, A. Comparative assessment of calcium aluminate cement and potassium-metakaolin-based geopolymer as binders in high-alumina refractories. *Cerâmica* **2025**, *71*, eMKWV7164. [CrossRef]
6. Consonni, L.; Luz, A.; Pandolfelli, V. Evaluation of the combined addition of aluminum lactate and calcium carbonate to alumina-based castables. *Cerâmica* **2021**, *67*, 196–202. [CrossRef]
7. Horckmans, L.; Nielsen, P.; Dierckx, P.; Ducastel, A. Recycling of refractory bricks used in basic steelmaking: A review. *Resour. Conserv. Recycl.* **2019**, *140*, 297–304. [CrossRef]
8. Hossain, S.; Roy, P. Fabrication of sustainable insulation refractory: Utilization of different wastes. *Bol. Soc. Esp. Ceram. Vidr.* **2019**, *58*, 115–125. [CrossRef]
9. Levinov, B.; D'yakov, V.; Krasnyi, B.; Kopeikin, V. A study of the chamotte materials produced using a dry aluminum–chromium phosphate binder. *Refractories* **1986**, *27*, 205–208. [CrossRef]
10. Bezerra, B.; Luz, A.; Pandolfelli, V. Novel drying additives and their evaluation for self-flowing refractory castables. *Ceram. Int.* **2020**, *46*, 3209–3217. [CrossRef]
11. Mathapati, P. An experimental investigation on behaviour of geo-polymer concrete slab with fly ash & GGBS under ambient curing. *Int. J. Res. Eng. Technol.* **2016**, *5*, 165–171. [CrossRef]
12. Minh, D.; Nhi, N.; Thang, N. Development of refractory synthesized from waste ceramic fiber and chamotte. *J. Polym. Compos.* **2020**, *8*, 101–109. [CrossRef]
13. Lima, L.; Silva, K.; Menezes, R.; Santana, L.; Lira, H. Microstructural characteristics, properties, synthesis and applications of mullite: A review. *Cerâmica* **2022**, *68*, 126–142. [CrossRef]
14. Coglitore, A.; Brentari, A.; Burresi, E.; Mazzanti, F.; Mingazzini, C.; Villa, M. Thermomechanical Behaviour of Alumina–Mullite Refractories Developed by Recycling Industrial Ceramic Wastes. In Proceedings of the Convegno Nazionale IGF XXII, Rome, Italy, 1–3 July 2013; pp. 43–47.
15. Stonys, R.; Malaiškienė, J.; Škamat, J.; Antonovič, V. Effect of hollow corundum microspheres additive on physical and mechanical properties and thermal shock resistance behavior of bauxite-based refractory castable. *Materials* **2021**, *14*, 4736. [CrossRef]
16. Mazzanti, F.; Brentari, A.; Burresi, E.; Coglitore, A.; Martelli, S.; Mingazzini, C.; Ricci, A.; Sangiorgi, S.; Scafe', M.; Villa, M. Exploitation of ceramic wastes by recycling in alumina–mullite refractories. *Adv. Sci. Technol.* **2010**, *70*, 9–14. [CrossRef]
17. Berjonneau, J.; Prigent, P.; Poirier, J. The Development of a Thermodynamic Model for Al_2O_3–MgO Refractory Castable Corrosion by Secondary Metallurgy Steel Ladle Slags. *Ceram. Int.* **2009**, *35*, 623–635. [CrossRef]
18. Patra, R.K.; Mukharjee, B.B. Influence of Incorporation of Granulated Blast Furnace Slag as Replacement of Fine Aggregate on Properties of Concrete. *J. Clean. Prod.* **2017**, *165*, 468–476. [CrossRef]
19. Karamanova, E.; Avdeev, G.; Karamanov, A. Ceramics from Blast Furnace Slag, Kaolin and Quartz. *J. Eur. Ceram. Soc.* **2011**, *31*, 989–998. [CrossRef]
20. Tiwari, A.; Singh, S.; Nagar, R. Feasibility Assessment for Partial Replacement of Fine Aggregate to Attain Cleaner Production Perspective in Concrete: A Review. *J. Clean. Prod.* **2016**, *135*, 490–507. [CrossRef]
21. Marinković, S.; Dragaš, J.; Ignjatović, I.; Tošić, N. Environmental assessment of green concretes for structural use. *J. Clean. Prod.* **2017**, *154*, 633–649. [CrossRef]
22. Jittin, V.; Bahurudeen, A.; Ajinkya, S. Utilisation of rice husk ash for cleaner production of different construction products. *J. Clean. Prod.* **2020**, *263*, 121578. [CrossRef]
23. Zharmenov, A.; Yefremova, S.; Satbaev, B.; Shalabaev, N.; Satbaev, S.; Yermishin, S.; Kablanbekov, A. Production of Refractory Materials Using a Renewable Source of Silicon Dioxide. *Minerals* **2022**, *12*, 1010. [CrossRef]
24. Antonovič, V.; Stonys, R.; Boris, R.; Malaiškienė, J. Effect of quartz sand on the properties and alkali resistance of refractory aluminosilicate castables. *Constr. Build. Mater.* **2022**, *351*, 128978. [CrossRef]
25. Xiang, R.; Li, Y.; Li, S.; Xue, Z.; He, Z.; Ouyang, S.; Nana, X. The potential usage of waste foundry sand from investment casting in refractory industry. *J. Clean. Prod.* **2019**, *211*, 1322–1327. [CrossRef]
26. De Lourdes Dos Santos Schackow, M.; Schackow, A.; Mundstock, K.; Folgueras, M. Sustainable silico-aluminous refractory wastes as an alternative raw material for hydraulic binder for foundry industry. *Clean. Mater.* **2024**, *11*, 100228. [CrossRef]

27. Bahtli, T.; Bostanci, V. Effect of precision casting sand waste of 4140 steel on the sintering and densification behaviour of chamotte refractories. *J. Therm. Anal. Calorim.* **2020**, *142*, 2385–2390. [CrossRef]
28. Iqbal, M.; Javed, M.; Rauf, M.; Azim, I.; Ashraf, M.; Yang, J.; Liu, Q. Sustainable utilization of foundry waste: Forecasting mechanical properties of foundry sand-based concrete using multi-expression programming. *Sci. Total Environ.* **2021**, *780*, 146524. [CrossRef]
29. Angulo-Ramírez, D.E.; Mejía de Gutiérrez, R.; Puertas, F. Alkali-activated Portland blast-furnace slag cement: Mechanical properties and hydration. *Constr. Build. Mater.* **2017**, *140*, 119–128. [CrossRef]
30. Li, Z.; Li, S. Carbonation resistance of fly ash and blast furnace slag-based geopolymer concrete. *Constr. Build. Mater.* **2018**, *163*, 668–680. [CrossRef]
31. Surul, O.; Bilir, T.; Gholampour, A.; Sutcu, M.; Ozbakkaloglu, T.; Gencel, O. Recycle of ground granulated blast furnace slag and fly ash on eco-friendly brick production. *Eur. J. Environ. Civ. Eng.* **2020**, *26*, 1738–1756. [CrossRef]
32. Teng, S.; Lim, T.Y.D.; Sabet Divsholi, B. Durability and mechanical properties of high strength concrete incorporating ultrafine ground granulated blast-furnace slag. *Constr. Build. Mater.* **2013**, *40*, 875–881. [CrossRef]
33. Chargui, F.; Hamidouche, M.; Belhouchet, H.; Jorand, Y.; Doufnoune, R.; Fantozzi, G. Mullite fabrication from natural kaolin and aluminium slag. *Bol. Soc. Esp. Ceram. Vidr.* **2018**, *57*, 169–177. [CrossRef]
34. Kumar, P.H.; Srivastava, A.; Kumar, V.; Majhi, M.R.; Singh, V.K. Implementation of industrial waste ferrochrome slag in conventional and low cement castables: Effect of microsilica addition. *J. Asian Ceram. Soc.* **2014**, *2*, 169–175. [CrossRef]
35. Kumar, P.H.; Srivastava, A.; Kumar, V.; Singh, V.K. Implementation of industrial waste ferrochrome slag in conventional and low cement castables: Effect of calcined alumina. *J. Asian Ceram. Soc.* **2014**, *2*, 371–379. [CrossRef]
36. Kurama, S.; Ozel, E. The influence of different CaO source in the production of anorthite ceramics. *Ceram. Int.* **2009**, *35*, 827–830. [CrossRef]
37. Boom Cárcamo, E.A.; Peñabaena-Niebles, R. Opportunities and Challenges for the Waste Management in Emerging and Frontier Countries through Industrial Symbiosis. *J. Clean. Prod.* **2022**, *363*, 132607. [CrossRef]
38. Das, D.; Rout, P.K. A Review of Coal Fly Ash Utilization to Save the Environment. *Water Air Soil Pollut.* **2023**, *234*, 61. [CrossRef]
39. Shukla, B.K.; Gupta, A.; Gowda, S.; Srivastav, Y. Constructing a Greener Future: A Comprehensive Review on the Sustainable Use of Fly Ash in the Construction Industry and Beyond. *Mater. Today Proc.* **2023**, *93*, 257–264. [CrossRef]
40. Nguyen, H.-H.T.; Nguyen, H.T.; Ahmed, S.F.; Rajamohan, N.; Yusuf, M.; Sharma, A.; Arunkumar, P.; Deepanraj, B.; Tran, H.-T.; Al-Gheethi, A.; et al. Emerging Waste-to-Wealth Applications of Fly Ash for Environmental Remediation: A Review. *Environ. Res.* **2023**, *227*, 115800. [CrossRef] [PubMed]
41. Liebermann, J. Reliability of Materials for High-Voltage Insulators. *Am. Ceram. Soc. Bull.* **2000**, *79*, 55–58.
42. Amigó, J.M.; Serrano, F.J.; Kojdecki, M.A.; Bastida, J.; Esteve, V.; Reventós, M.M. X-Ray Diffraction Microstructure Analysis of Mullite, Quartz and Corundum in Porcelain Insulators. *J. Eur. Ceram. Soc.* **2005**, *25*, 1479–1486. [CrossRef]
43. Gubanski, S. Outdoor High Voltage Insulation. *IEEE Trans. Dielectr. Electr. Insul.* **2010**, *17*, 325. [CrossRef]
44. Meng, Y.; Gong, G.; Wu, Z.; Yin, Z.; Xie, Y.; Liu, S. Fabrication and Microstructure Investigation of Ultra-High-Strength Porcelain Insulator. *J. Eur. Ceram. Soc.* **2012**, *32*, 3043–3049. [CrossRef]
45. Contreras, J.E.; Rodríguez, E.A. Nanostructured Insulators—A Review of Nanotechnology Concepts for Outdoor Ceramic Insulators. *Ceram. Int.* **2017**, *43*, 8545–8550. [CrossRef]
46. Ogbonda, C.; Onuchuku, P. Enhancement of Mechanical and Dielectric Properties of Porcelain Insulators Using Locally Available Raw Materials. *BW Acad. J.* **2023**, 14. Available online: https://bwjournal.org/index.php/bsjournal/article/view/1314 (accessed on 18 June 2023).
47. Addis, T.; Wondemagegnehu, E.B.; Zereffa, E.A.; Tullu, A.M.; Brehane, B. Sugarcane Bagasse Ash Substituent Feldspar for the Production of Porcelain Electrical Insulators. *Ceram. Int.* **2023**, *49*, 7727–7736. [CrossRef]
48. Harper, C. *Handbook of Ceramics, Glasses, and Diamonds*; McGraw-Hill Professional: Sydney, Australia, 2001.
49. Bragança, S.R.; Bergman, C.P. Microestrutura e Propriedades de Porcelanas. *Cerâmica* **2004**, *50*, 291–299. [CrossRef]
50. Dana, K.; Das, S.; Das, K.S. Effect of Substitution of Fly Ash for Quartz in Triaxial Kaolin–Quartz–Feldspar System. *J. Eur. Ceram. Soc.* **2004**, *24*, 3169–3175. [CrossRef]
51. Sánchez, E.; García-Ten, J.; Sanz, V.; Moreno, A. Porcelain Tile: Almost 30 Years of Steady Scientific-Technological Evolution. *Ceram. Int.* **2010**, *36*, 831–845. [CrossRef]
52. Liebermann, J. *High-Voltage Insulators: Basics and Trends for Producers, Users and Students*; Fraunhofer Institute for Ceramic Technologies and Systems IKTS: Dresden, Germany, 2012.
53. Piva, D.H.; Piva, R.H.; Venturini, J.; Ramon, J.; Caldas, V.; Morelli, M.R.; Bergmann, C. Effect of Fe_2O_3 Content on the Electrical Resistivity of Aluminous Porcelain Applied to Electrical Insulators. *Ceram. Int.* **2016**, *42*, 5045–5052. [CrossRef]
54. Owoeye, S.S.; Toludare, T.S.; Isinkaye, O.E.; Kingsley, U. Influence of Waste Glasses on the Physico-Mechanical Behavior of Porcelain Ceramics. *Bol. Soc. Esp. Ceram. Vidr.* **2019**, *58*, 77–84. [CrossRef]

55. GlobalData Energy. Tracking the Growth of the Global Power Insulator Market, 2018–2022. Power Technology. 2022. Available online: https://www.power-technology.com/comment/tracking-growth-global-power-insulator-market (accessed on 10 January 2024).
56. Kaviraj, A.K.; Saha, S.; Chakraborty, A.; Pahari, G.; Ray, D.; Parya, T.K.; Das, S.K. Differences in Phase, Microstructural, and Electrical Characteristics of Quartz-Substituted Alumina Porcelain Insulator. *J. Australas. Ceram. Soc.* **2020**, *57*, 327–337. [CrossRef]
57. Pereira, V.M.; Geraldo, R.H.; Baldusco, R.; Camarini, G. Porcelain Waste from Electrical Insulators in Self-Leveling Mortar: Materials Characterization and Properties. *J. Build. Eng.* **2022**, *61*, 105297. [CrossRef]
58. Naenudon, S.; Wongsa, A.; Ekprasert, J.; Sata, V.; Chindaprasirt, P. Enhancing the Properties of Fly Ash-Based Geopolymer Concrete Using Recycled Aggregate from Waste Ceramic Electrical Insulator. *J. Build. Eng.* **2023**, *68*, 106132. [CrossRef]
59. Liu, T.; Zhang, J.; Wu, J.; Liu, J.; Li, C.; Ning, T.; Luo, Z.; Zhou, X.; Yang, Q.; Lu, A. The Utilization of Electrical Insulators Waste and Red Mud for Fabrication of Partially Vitrified Ceramic Materials with High Porosity and High Strength. *J. Clean. Prod.* **2019**, *223*, 790–800. [CrossRef]
60. Campos, M.A.; Paulon, V.A.; De Argollo Ferrao, A.M. Concrete Made with Alternative Fine Aggregates: The Reuse of Porcelain Electrical Insulators. *Mater. Sci. Forum* **2018**, *912*, 185–190. [CrossRef]
61. Pivak, A.; Pavlíková, M.; Zaleská, M.; Lojka, M.; Lauermannová, A.-M.; Jankovský, O.; Pavlík, Z. Low-Carbon Composite Based on MOC, Silica Sand and Ground Porcelain Insulator Waste. *Processes* **2020**, *8*, 829. [CrossRef]
62. Pereira, V.M.; Camarini, G. Fresh and Hardened Properties of Self-Leveling Mortars with Porcelain and Red Ceramic Wastes. *Adv. Civ. Eng.* **2018**, *2018*, 6378643. [CrossRef]
63. Garg, N.; Shrivastava, S. Mechanical, Durability and Sustainability Assessment of Rendering Mortar with Synergistic Utilisation of Recycled Concrete and Ceramic Insulator Fine Aggregates. *J. Build. Eng.* **2023**, *76*, 107269. [CrossRef]
64. Xu, N.; Li, S.; Li, Y.; Xue, Z.; Yuan, L.; Zhang, J.; Wang, L. Preparation and Properties of Porous Ceramic Aggregates Using Electrical Insulators Waste. *Ceram. Int.* **2015**, *41*, 5807–5811. [CrossRef]
65. *ASTM-C860*; Standard Practice for Determining the Consistency of Refractory Castable Using the Ball-in-Hand Test. ASTM International: West Conshohocken, PA, USA, 2000; pp. 1–5.
66. *ASTM-C865*; Standard Practice for Firing Refractory Concrete Specimens. ASTM International: West Conshohocken, PA, USA, 2002; pp. 1–3.
67. *ASTM-C20*; Standard Test Methods for Apparent Porosity, Water Absorption, Apparent Specific Gravity, and Bulk Density of Burned Refractory Brick and Shapes by Boiling Water. ASTM International: West Conshohocken, PA, USA, 2000; pp. 1–3.
68. *ASTM-C133*; Standard Test Methods for Cold Crushing Strength and Modulus of Rupture of Refractories. ASTM International: West Conshohocken, PA, USA, 1997; pp. 1–6.
69. Liu, Y.; Yin, H.; Tang, Y.; Xin, Y.; Yuan, H.; Ren, X.; Wan, Q. Synthesis Mechanism and Properties of Lightweight Mullite–Corundum Refractories Obtained through High Temperature Liquid-Assisted Micrometer-Scale Kirkendall Effect. *Ceram. Int.* **2021**, *47*, 9234–9244. [CrossRef]
70. You, Q.; Wu, Z.; Li, Y.; Zhong, Y.; Shang, S.; Yuan, M.; Ou, Y.; Xu, H.; Cui, S. Amorphous SiOC-Coated Submicron Mullite Aerogels with Excellent Thermal and Structural Stability up to 1500 °C. *J. Eur. Ceram. Soc.* **2024**, *45*, 117079. [CrossRef]
71. Xu, X.; Shen, Y.; Wu, J.; Qiu, S.; Yu, J.; Zhou, Y. Effect of Different Silicon Sources on the Properties of In-Situ Synthesized Corundum–Mullite Composite Thermal Storage Ceramics. *Ceram. Int.* **2024**, *50*, 17043–17053. [CrossRef]
72. Kenzhaliyev, B.; Biryukova, A.; Dzhienalyev, T.; Panichkin, A.; Imbarova, A.; Uskenbaeva, A.; Yusoff, A.H. Assessment of Microsilica as a Raw Material for Obtaining Mullite–Silica Refractories. *Processes* **2024**, *12*, 200. [CrossRef]
73. Ondro, T.; Al-Shantir, O.; Csáki, I.; Lukáč, F.; Trník, A. Kinetic Analysis of Sinter-Crystallization of Mullite and Cristobalite from Kaolinite. *Thermochim. Acta* **2019**, *678*, 178312. [CrossRef]
74. Sainz, M.; Serrano, F.; Bastida, J.; Caballero, A. Microstructural Evolution and Growth of Crystallite Size of Mullite during Thermal Transformation of Kyanite. *J. Eur. Ceram. Soc.* **1997**, *17*, 1277–1284. [CrossRef]
75. Yu, P.; Tsai, Y.; Yen, F.; Huang, C. Thermal Reaction of Cristobalite in Nano-SiO_2/Al_2O_3 Powder Systems for Mullite Synthesis. *J. Am. Ceram. Soc.* **2014**, *97*, 2431–2438. [CrossRef]
76. Barrientos-Hernández, F.R.; Pérez-Labra, M.; Lobo-Guerrero, A.; Reyes-Pérez, M.; Juárez-Tapia, J.C.; Hernández-Ávila, J.; Cardoso-Legorreta, E.; Hernández-Lara, J. Effect of Particle Size and Sintering Temperature on the Formation of Mullite from Kyanite and Aluminum Mixtures. *Adv. Mater. Sci. Eng.* **2021**, *2021*, 6678297. [CrossRef]
77. Zhai, K.; Xue, W.; Wang, H.; Wu, X.; Zhai, S. Raman Spectra of Sillimanite, Andalusite, and Kyanite at Various Temperatures. *Phys. Chem. Miner.* **2020**, *47*, 23. [CrossRef]
78. He, Q.; Liu, X.; Li, B.; Deng, L.; Liu, W.; Wang, L. Thermal Equation of State of a Natural Kyanite up to 8.55 GPa. *Matter Radiat. Extremes* **2016**, *1*, 269–276. [CrossRef]
79. Nemaleu, J.G.D.; Kaze, C.R.; Belela, E.A.; Lecomte-Nana, G.; Kamseu, E.; Sglavo, V.; Leonelli, C. Refractory Ceramics Bonds from Potassium-Based Inorganic Polymer for Advanced Applications: Crystalline Phase Changes and Descriptive Microstructure. *Ceram. Int.* **2022**, *48*, 21579–21588. [CrossRef]

80. Lin, S.; Yu, Y.; Zhong, M.; Yang, H.; Liu, Y.; Li, H.; Zhang, C.Y.; Zhang, Z.J. Preparation of Anorthite/Mullite In Situ and Phase Transformation in Porcelain. *Materials* **2023**, *16*, 416. [CrossRef] [PubMed]
81. Li, C.; Chao, B.; Han, Y.; Wang, C.; An, L. Mullite Whisker Reinforced Porous Anorthite Ceramics with Low Thermal Conductivity and High Strength. *J. Eur. Ceram. Soc.* **2016**, *36*, 761–765. [CrossRef]
82. Ryu, H.; Kasai, E.; Saito, F. Effect of Mixed Grinding of Kaolinite–Gibbsite Mixture on Formation of Mullite. *Shigen-to-Sozai* **1992**, *108*, 221–226. [CrossRef]
83. Taşkıran, F.; Kalpaklı, Y. In Situ Boro-Mullite Phase Formation in Glass–Ceramic Glazes: Anatase–Rutile Phase Transformations and Microstructure Properties. *Ceram. Int.* **2024**, *50*, 50667–50679. [CrossRef]
84. Wallez, G.; Bouquillon, A.; Coquinot, Y. Thermal Evolution of a Kaolin: Quantitative Phase Analysis and Assessment of the Thermal Markers of the Provins Clay. *Appl. Clay Sci.* **2024**, *261*, 107582. [CrossRef]
85. Wang, H.; Li, B.; He, M.; Hwang, J.Y. Mullitization Characteristics and Sinterability of Kyanite in Ceramic Preparation. In *Characterization of Minerals, Metals, and Materials 2017*; Springer: Cham, Switzerland, 2017; pp. 251–259. [CrossRef]
86. Schneider, H.; Majdič, A. Kinetics of the Thermal Decomposition of Kyanite. *Ceramurgia Int.* **1980**, *6*, 61–66. [CrossRef]
87. Lin, Y.-M.; Li, C.-W.; Wang, C.-A. Effects of Mullite Content on the Properties and Microstructure of Porous Anorthite/Mullite Composite Ceramics. *J. Inorg. Mater.* **2011**, *26*, 1095–1100. [CrossRef]
88. Lin, Y.-M.; Li, C.-W.; Yang, F.-K.; Wang, C.-A. Preparation and Properties of Porous Anorthite–Mullite Ceramics. *Key Eng. Mater.* **2012**, *512–515*, 590–595. [CrossRef]
89. Frost, R.; Kloprogge, J.; Russell, S.; Szetu, J. Vibrational Spectroscopy and Dehydroxylation of Aluminum (Oxo)Hydroxides: Gibbsite. *Appl. Spectrosc.* **1999**, *53*, 423–434. [CrossRef]
90. Ingram-Jones, V.J.; Slade, R.; Davies, T.; Southern, J.; Salvador, S. Dehydroxylation Sequences of Gibbsite and Boehmite: Study of Differences between Soak and Flash Calcination and of Particle-Size Effects. *J. Mater. Chem.* **1996**, *6*, 73–79. [CrossRef]
91. Djaida, R.D.R.; Foudil, S.F.S. Kinetics Parameters of the Thermal Dehydroxylation of Gibbsite $Al(OH)_3$ by Differential Thermal Analysis (DTA). *J. Mater. Environ. Sci.* **2016**, *5*, 7–12.
92. Zhu, B.; Fang, B.; Li, X. Dehydration Reactions and Kinetic Parameters of Gibbsite. *Ceram. Int.* **2010**, *36*, 2493–2498. [CrossRef]
93. Namiranian, A.; Kalantar, M. Mullite Synthesis and Formation from Kyanite Concentrates in Different Conditions of Heat Treatment and Particle Size. *Iran. J. Mater. Sci. Eng.* **2011**, *8*, 29–36.
94. Abolhasani, A.; Samali, B.; Aslani, F. Physicochemical, Mineralogical, and Mechanical Properties of Calcium Aluminate Cement Concrete Exposed to Elevated Temperatures. *Materials* **2021**, *14*, 3855. [CrossRef] [PubMed]
95. Geng, G.; Li, J.; Yu, Y.S.; Shapiro, D.; Kilcoyne, D.; Monteiro, P. Nanometer-Resolved Spectroscopic Study Reveals the Conversion Mechanism of $CaO{\cdot}Al_2O_3{\cdot}10H_2O$ to $2CaO{\cdot}Al_2O_3{\cdot}8H_2O$ and $3CaO{\cdot}Al_2O_3{\cdot}6H_2O$ at an Elevated Temperature. *Cryst. Growth Des.* **2017**, *17*, 4246–4253. [CrossRef]
96. Zapata, J.; Colorado, H.; Gómez, M. Effect of High Temperature and Additions of Silica on the Microstructure and Properties of Calcium Aluminate Cement Pastes. *J. Sustain. Cem.-Based Mater.* **2020**, *9*, 323–349. [CrossRef]
97. Aguilar-Santillan, J.; Cuenca-Álvarez, R.; Balmori-Ramírez, H.; Bradt, R. Mechanical Activation of the Decomposition and Sintering of Kyanite. *J. Am. Ceram. Soc.* **2002**, *85*, 2425–2431. [CrossRef]
98. Kashcheev, I.; Ust'yantsev, V.M.; Sychev, S.N. Kyanite Concentrate of the Karabash Deposit: Phase Transformations during Heating. *Refract. Ind. Ceram.* **2007**, *48*, 250–254. [CrossRef]
99. Zhang, Y.; Chang, J.; Ji, J. AH_3 Phase in the Hydration Product System of AFt–AFm–AH_3 in Calcium Sulfoaluminate Cements: A Microstructural Study. *Constr. Build. Mater.* **2018**, *167*, 587–596. [CrossRef]
100. Irisawa, K.; García-Lodeiro, I.; Kinoshita, H. Influence of Mixing Solution on Characteristics of Calcium Aluminate Cement Modified with Sodium Polyphosphate. *Cem. Concr. Res.* **2020**, *137*, 105951. [CrossRef]
101. Pacewska, B.; Nowacka, M. Studies of Conversion Progress of Calcium Aluminate Cement Hydrates by Thermal Analysis Method. *J. Therm. Anal. Calorim.* **2014**, *117*, 653–660. [CrossRef]
102. Vasile, B.; Dobra, G.; Iliev, S.; Cotet, L.; Neacșu, I.; Surdu, V.A.; Nicoară, A.; Boiangiu, A.; Filipescu, L. Thermally Activated $Al(OH)_3$. Part II—Effect of Different Thermal Treatments. *Ceramics* **2021**, *4*, 40. [CrossRef]
103. Kitamura, M.; Senna, M. Effects of Preheating on Mechanochemical Amorphization and Enhanced Reactivity of Aluminum Hydroxide. *Adv. Powder Technol.* **2001**, *12*, 215–226. [CrossRef]
104. Eisinas, A.; Dambrauskas, T.; Baltakys, K.; Ruginytė, K. The Peculiarities of Mayenite Formation from Synthetic Katoite and Calcium Monocarboaluminate Samples in the Temperature Range 25–1150 °C. *J. Therm. Anal. Calorim.* **2019**, *138*, 2275–2282. [CrossRef]
105. Das, S.; Mitra, A.; Poddar, P.K.D. Thermal Analysis of Hydrated Calcium Aluminates. *J. Therm. Anal.* **1996**, *47*, 765–774. [CrossRef]
106. Salasin, J.; Rawn, C. In-Situ Kinetic Investigation of Calcium Aluminate Formation. *Ceramics* **2018**, *1*, 16. [CrossRef]
107. Abd-El-Raoof, F.; Youssef, H.; El-Sokkary, T.; El-Shakour, Z.A.A.; Tawfik, A.Y. Fabrication and Characterization of Calcium Aluminate Cement via Microwave-Hydrothermal Route: Mayenite, Katoite, and Hydrocalumite. *Constr. Build. Mater.* **2023**, *369*, 132988. [CrossRef]

108. Khaliq, W.; Khan, H.A. High Temperature Material Properties of Calcium Aluminate Cement Concrete. *Constr. Build. Mater.* **2015**, *94*, 475–487. [CrossRef]
109. Salomão, R.; Kawamura, M.; Emilio, A.B.; Sakihama, J.; Segadães, A.M. Calcium Aluminate Cement in Castable Alumina: From Hydrate Bonding to the In Situ Formation of Calcium Hexaluminate. *Ceram. Int.* **2021**, *47*, 3668–3678. [CrossRef]
110. Koplík, J.; Švec, J.; Másilko, J.; Sedlačík, M.; Bartoníčková, E. Synthesis of Calcium Aluminate Hydrates, Their Characterization and Dehydration. *Ceram. Int.* **2024**, *51*, 5536–5543. [CrossRef]
111. Lin, P.X.; Zhang, D.; Yan, W.; Yu, H.Y. Synthesis and Characterization of Calcium Aluminate Compounds from Gehlenite by High-Temperature Solid-State Reaction. *Ceram. Int.* **2018**, *44*, 10241–10249. [CrossRef]
112. Zuluaga, C.A.; Ríos, C.A.; Castellanos, O. Early Paleozoic and Jurassic Orogenic Events in the Northern Andes: Evidence from Polymetamorphism in a Kyanite–Andalusite–Sillimanite Crystallization Sequence. *Geol. Soc. Lond. Spec. Publ.* **2025**, *558*, 121. [CrossRef]
113. Whitney, D. Coexisting Andalusite, Kyanite, and Sillimanite: Sequential Formation of Three Al_2SiO_5 Polymorphs during Progressive Metamorphism near the Triple Point, Sivrihisar, Turkey. *Am. Miner.* **2002**, *87*, 405–416. [CrossRef]
114. Tsuneyuki, S.; Aoki, H.; Tsukada, M.; Matsui, Y. Molecular-Dynamics Study of the Alpha to Beta Structural Phase Transition of Quartz. *Phys. Rev. Lett.* **1990**, *64*, 776–779. [CrossRef]
115. Ranieri, V.; Bourgogne, D.; Darracq, S.; Cambon, M.; Haines, J.; Cambon, O.; Leparc, R.; Levelut, C.; Largeteau, A.; Demazeau, G. Raman Scattering Study of α-Quartz and $Si_{1-x}Ge_xO_2$ Solid Solutions. *Phys. Rev. B* **2009**, *79*, 224304. [CrossRef]
116. Murri, M.; Prencipe, M. Anharmonic Effects on the Thermodynamic Properties of Quartz from First-Principles Calculations. *Entropy* **2021**, *23*, 1366. [CrossRef] [PubMed]
117. Kohn, M. A Refined Zirconium-in-Rutile Thermometer. *Am. Miner.* **2020**, *105*, 963–971. [CrossRef]
118. Mechri, M.L.; Chihi, S.; Mahdadi, N.; Beddiaf, S. Study of Heat Effect on the Composition of Dunes Sand of Ouargla (Algeria) Using XRD and FTIR. *Silicon* **2017**, *9*, 933–941. [CrossRef]
119. Zhou, H.; Qiao, X.; Yu, J. Influences of Quartz and Muscovite on the Formation of Mullite from Kaolinite. *Appl. Clay Sci.* **2013**, *80*, 176–181. [CrossRef]
120. Rana, A.; Aiko, O.; Pask, J.A. Sintering of α-Al_2O_3/Quartz and α-Al_2O_3/Cristobalite Related to Mullite Formation. *Ceram. Int.* **1982**, *8*, 151–153. [CrossRef]
121. Garcia-Valles, M.; Cuevas, D.; Alfonso, P.; Martínez, S. Thermal Behaviour of Ceramics Obtained from the Kaolinitic Clays of Terra Alta, Catalonia, Spain. *J. Therm. Anal. Calorim.* **2022**, *147*, 5303–5312. [CrossRef]
122. Zhang, J.; Jia, Q.; Yan, S.; Zhang, S.; Liu, X. Microstructure and Properties of Hydratable Alumina Bonded Bauxite–Andalusite Based Castables. *Ceram. Int.* **2016**, *42*, 310–316. [CrossRef]
123. Stjernberg, J.; Lindblom, B.; Wikström, J.; Antti, M.-L.; Odén, M. Microstructural Characterization of Alkali Metal Mediated High Temperature Reactions in Mullite Based Refractories. *Ceram. Int.* **2010**, *36*, 733–740. [CrossRef]
124. Maldhure, A.V.; Tripathi, H.S.; Ghosh, A. Mechanical Properties of Mullite–Corundum Composites Prepared from Bauxite. *Int. J. Appl. Ceram. Technol.* **2015**, *12*, 860–866. [CrossRef]
125. Zare, S.; Monshi, A.; Saidi, A. Improving In Situ Spinel Refractory Castables Using a Novel Binder. *Ceram. Int.* **2016**, *42*, 5885–5896. [CrossRef]
126. Liu, Y.; Xu, L.; Chen, M.; Zhang, D. Effects of Andalusite and Kyanite Addition on the Microstructure, Thermo-Mechanical Properties and Corrosion Resistance of Ultralow-Cement Bauxite–Corundum Castables. *Ceram. Int.* **2022**, *48*, 14141–14150. [CrossRef]
127. Andreeva, O.V. Calculation of the Concentration of Chamotte in Ceramics: New Experimental Data. *Vestn. Novosib. State Univ. Ser. Hist. Philol.* **2024**, *23*, 35–42. [CrossRef]
128. McNutt, P.F.; Sood, S.S.; Brandvold, A.S.; Ozer, A.; Kriven, W. Optimizing the Design Parameters for Chamotte Particle-Reinforced Geopolymers. *J. Am. Ceram. Soc.* **2024**, *107*, 6045–6059. [CrossRef]
129. Gu, W.; Zhu, L.; Shang, X.; Ding, D.; Liu, L.; Chen, L.; Ye, G. Effect of particle size of calcium aluminate cement on volumetric stability and thermal shock resistance of CAC-bonded castables. *J. Alloys Compd.* **2019**, *772*, 637–641. [CrossRef]
130. Bareiro, W.G.; De Andrade Silva, F.; Sotelino, E.D.; Gomes, O.D.F.M. The influence of alumina content on the chemical and mechanical behavior of refractory concretes fired at different temperatures. *Constr. Build. Mater.* **2018**, *187*, 1214–1223. [CrossRef]
131. Zapata, J.; Azevedo, A.; Fontes, C.; Monteiro, S.; Colorado, H. Environmental impact and sustainability of calcium aluminate cements. *Sustainability* **2022**, *14*, 2751. [CrossRef]
132. De Sousa, L.L.; Salomão, R.; Arantes, V.L. Development and characterization of porous moldable refractory structures of the alumina–mullite–quartz system. *Ceram. Int.* **2017**, *43*, 1362–1370. [CrossRef]
133. Pan, L.; He, Z.; Li, Y.; Zhu, T.; Wang, Q.; Li, B. Effects of cement content on the microstructural evolution and mechanical properties of cement-bonded corundum castables. *Ceram. Int.* **2020**, *46*, 4634–4642. [CrossRef]
134. Gao, S.; Zhang, P.; Li, N.; Zhang, J.; Luan, J.; Ye, G.; Liao, G. Effect of CAC content on the strength of castables at temperatures between 300 and 1000 °C. *Ceram. Int.* **2020**, *46*, 14957–14963. [CrossRef]

135. Zhang, P.; Li, N.; Luan, J.; Gao, S.; Ye, G. Relationship between the strength and microstructure of CAC-bonded castables under intermediate temperatures. *Ceram. Int.* **2020**, *46*, 888–892. [CrossRef]
136. Cultrone, G.; Sebastián, E.; Elert, K.; De la Torre, M.; Cazalla, O.; Navarro, C. Influence of Mineralogy and Firing Temperature on the Porosity of Bricks. *J. Eur. Ceram. Soc.* **2004**, *24*, 547–564. [CrossRef]
137. Khater, G.; Romero, M.; López-Delgado, A.; Padilla, I.; El-Kheshen, A.A.; Farag, M.M.; Elmaghraby, M.S.; Nasralla, N.; Shendy, H. Novel Ceramic Materials Based on Industrial Wastes within the CaO–MgO–Al_2O_3–SiO_2 System. *Mater. Chem. Phys.* **2024**, *331*, 130178. [CrossRef]
138. Sarpoolaky, H.; Ahari, K.G.; Lee, W.E. Influence of in situ phase formation on microstructural evolution and properties of castable refractories. *Ceram. Int.* **2002**, *28*, 487–493. [CrossRef]
139. Hossain, S.S.; Roy, P.K. Waste rice husk ash derived sol: A potential binder in high alumina refractory castables as a replacement of hydraulic binder. *J. Alloys Compd.* **2020**, *817*, 152806. [CrossRef]
140. Badioli, S.; Jubayed, M.; Dargaud, M.; Siebring, R.; Léonard, A. Environmental performance of refractories: A state-of-the-art review on current methodological practices and future directions. *Environ. Sustain. Indic.* **2025**, *27*, 100868. [CrossRef]
141. Kurovics, E.; Ibrahim, J.F.M.; Tihtih, M.; Udvardi, B.; Nuilek, K.; Gömze, L.A. Examination of mullite ceramic specimens made by conventional casting method from kaolin and sawdust. *J. Phys. Conf. Ser.* **2020**, *1527*, 012034. [CrossRef]
142. Mandal, B.; Sarkar, R.; Daspoddar, P.K. Effect of different mullite precursors on the properties of low cement high alumina castable. *Ind. Ceram.* **2011**, *31*, 217–222.
143. Quanli, J.; Ju, Z.; Ying, Z.; Gaoyang, J.; Xinhong, L. Effect of microsilica addition on the properties of colloidal silica bonded bauxite–andalusite based castables. *Ceram. Int.* **2018**, *44*, 3064–3068. [CrossRef]
144. Koehler, A.; Rößler, C.; Neubauer, J.; Goetz-Neunhoeffer, F. Phase and Porosity Changes in a Calcium Aluminate Cement and Alumina System under Hydrothermal Conditions. *Ceram. Int.* **2022**, *48*, 18873–18883. [CrossRef]
145. Shirani, S.; Cuesta, A.; Torre, G.; Diaz, A.; Trtik, P.; Holler, M.; Aranda, M. Calcium Aluminate Cement Conversion Analysed by Ptychographic Nanotomography. *Cem. Concr. Res.* **2020**, *137*, 106201. [CrossRef]
146. Romero, M.; Andrés, A.; Alonso, R.; Viguri, J.; Rincón, J. Sintering Behaviour of Ceramic Bodies from Contaminated Marine Sediments. *Ceram. Int.* **2008**, *34*, 1917–1924. [CrossRef]
147. Zan, W.; Ma, B.; Chen, G.; Cao, C.; Li, M.; Wang, Y.; Shen, H. Preparation and Properties of Mullite Ceramic-Based Porous Aggregates with High Closed Porosity Utilizing Low-Voltage Electroceramics Waste. *Constr. Build. Mater.* **2024**, *392*, 136943. [CrossRef]
148. Lu, P.K.; Xu, X.; Yi, W.; German, R. Porosity Effect on Densification and Shape Distortion in Liquid Phase Sintering. *Mater. Sci. Eng. A* **2001**, *318*, 111–121. [CrossRef]
149. Low, R.; Robertson, I.; Schaffer, G. Excessive Porosity after Liquid-Phase Sintering of Elemental Titanium Powder Blends. *Scr. Mater.* **2007**, *56*, 895–898. [CrossRef]
150. Young, E. High Density Supersolidus Liquid Phase Sintering of Steel Powders. Ph.D. Thesis, The University of British Columbia, Vancouver, BC, Canada, 2002. [CrossRef]
151. Firoozjaei, E.A.; Saidi, A.; Monshi, A.; Koshy, P. The effect of microsilica and refractory cement content on the properties of andalusite-based low cement castables used in aluminum casthouse. *Cerâmica* **2010**, *56*, 411–421. [CrossRef]
152. Hou, X.; Chen, J.; Cao, Y.; Liu, G.; Wei, G.; Yan, W.; Wei, Y.; Li, N.; Zhang, Y. Influence of bonding systems on the properties of Al_2O_3–MgO refractory castables: Aluminate cement and alumina silica gel. *Ceram. Int.* **2024**, *50*, 46695–46704. [CrossRef]
153. Consonni, L.B.; Luz, A.P.; Pandolfelli, V.C. Binding additives with sintering action for high-alumina based castables. *Ceram. Int.* **2019**, *45*, 15290–15297. [CrossRef]
154. Krishnan, M.; Manikandan, R.; Thenmuhil, D. Effect of heat treatment and zircon addition on the properties of low-cement castables based on recycled alumina grog. *Ceram. Int.* **2021**, *47*, 3430–3443. [CrossRef]
155. Ferreira, G.; López-Sabirón, A.M.; Aranda, J.; Mainar-Toledo, M.D.; Aranda-Usón, A. Environmental Analysis for Identifying Challenges to Recover Used Reinforced Refractories in Industrial Furnaces. *J. Clean. Prod.* **2015**, *88*, 242–253. [CrossRef]
156. Korai, H.; Saotome, H.; Ohmi, M. Effects of Water Soaking and Outdoor Exposure on Modulus of Rupture and Internal Bond Strength of Particleboard. *J. Wood Sci.* **2014**, *60*, 127–133. [CrossRef]
157. Korai, H.; Adachi, K.; Saotome, H. Deterioration of Wood-Based Boards Subjected to Outdoor Exposure in Tsukuba. *J. Wood Sci.* **2013**, *59*, 24–34. [CrossRef]
158. Jun, D.; Yu, C.; Jianpeng, L.; Deng, C.; Xi Zhu, H. Effects of Silicon Powder Content on the Properties and Interface Bonding of Nitrided Al_2O_3–C Refractories. *Mater. Chem. Phys.* **2018**, *206*, 193–203. [CrossRef]
159. Zhu, B.; Zhu, Y.; Li, X.; Zhao, F. Effect of Ceramic Bonding Phases on the Thermo-Mechanical Properties of Al_2O_3–C Refractories. *Ceram. Int.* **2013**, *39*, 6069–6076. [CrossRef]
160. Yanshan, L.; Han, B.; Zhang, T.; Yu, H.; Yan, W.; Wu Wei, Y.; Li, N. Effect of Zirconia Particle Size on the Properties of Alumina–Spinel Castables. *Ceram. Int.* **2016**, *42*, 16961–16968. [CrossRef]

161. Lu, J.; Zhang, Z.; Li, Y.; Liu, Z. Effect of Alumina Source on the Densification, Phase Evolution, and Strengthening of Sintered Mullite-Based Ceramics from Milled Coal Fly Ash. *Constr. Build. Mater.* **2019**, *229*, 116851. [CrossRef]
162. Zheng, M.; Li, N.; Yan, W. Effect of Sintering Temperature on the Phase Composition and Microstructure of Anorthite–Mullite–Corundum Porous Ceramics. *Ceram. Int.* **2014**, *40*, 15795–15799. [CrossRef]
163. Grabias-Blicharz, E.; Franus, W. A Critical Review on Mechanochemical Processing of Fly Ash and Fly Ash-Derived Materials. *Sci. Total Environ.* **2023**, *860*, 160529. [CrossRef] [PubMed]
164. Bezerra, B.P.; Luz, A.P. Geopolymers: A Viable Binder Option for Ultra-Low-Cement and Cement-Free Refractory Castables? *J. Eur. Ceram. Soc.* **2024**, *44*, 5241–5251. [CrossRef]
165. Krasnyi, B.L.; Ikonnikov, K.I.; Lemeshev, D.O.; Sizova, A.S. Fly Ash as Technogenic Raw Material for Producing Refractory and Insulating Ceramic Materials (Review). *Glass Ceram.* **2021**, *78*, 48–56. [CrossRef]
166. Mathapati, M.; Amate, K.; Durga Prasad, C.; Jayavardhana, M.L.; Hemanth Raju, T. A Review on Fly Ash Utilization. *Mater. Today Proc.* **2022**, *50*, 1535–1540. [CrossRef]

Disclaimer/Publisher's Note: The statements, opinions and data contained in all publications are solely those of the individual author(s) and contributor(s) and not of MDPI and/or the editor(s). MDPI and/or the editor(s) disclaim responsibility for any injury to people or property resulting from any ideas, methods, instructions or products referred to in the content.